



http://dx.doi.org/10.1016/j.ultrasmedbio.2017.02.020

Original Contribution

PREDICTING TISSUE SUSCEPTIBILITY TO MECHANICAL CAVITATION DAMAGE IN THERAPEUTIC ULTRASOUND

Lauren Mancia,* Eli Vlaisavljevich,† Zhen Xu,†‡ and Eric Johnsen*

*Department of Mechanical Engineering, University of Michigan, Ann Arbor, Michigan, USA; †Department of Biomedical Engineering, University of Michigan, Ann Arbor, Michigan, USA; and †Division of Pediatric Cardiology, Department of Pediatrics and Communicable Diseases, University of Michigan, Ann Arbor, Michigan, USA

(Received 24 October 2016; revised 14 February 2017; in final form 28 February 2017)

Abstract—Histotripsy is a developing focused ultrasound procedure that uses cavitation bubbles to mechanically homogenize soft tissue. To better understand the mechanics of tissue damage, a numerical model of single-bubble dynamics was used to calculate stress, strain and strain rate fields produced by a cavitation bubble exposed to a tensile histotripsy pulse. The explosive bubble growth and its subsequent collapse were found to depend on the properties of the surrounding material and on the histotripsy pulse. Stresses far greater than gigapascals were observed close to the bubble wall, but attenuated by four to six orders of magnitude within 50 μ m from the bubble wall, with at least two orders of magnitude attenuation occurring within the first 10 μ m from the bubble. Elastic stresses were found to dominate close to the bubble wall, whereas viscous stresses tended to persist farther into the surroundings. A non-dimensional parameter combining tissue, waveform and bubble properties was identified that dictates the dominant stress (viscous vs. elastic) as a function of distance from the bubble nucleus. In a cycle of bubble growth and collapse, characteristic times at which mechanical damage is likely to occur and dominant mechanisms acting at each time were identified. (E-mail: lamancha@umich.edu) © 2017 World Federation for Ultrasound in Medicine & Biology.

Key Words: Cavitation, Bubble dynamics, Simulation, Histotripsy, Tissue ablation.

INTRODUCTION

High-intensity ultrasound pulses produce rapid pressure changes in tissue, thus giving rise to cavitation. As they grow and collapse, bubbles forming in low-pressure regions can cause damage to surrounding tissue. Acoustic cavitation dynamics in soft tissue has been a subject of growing interest since the development of non-invasive, focused ultrasound therapies. Treatments such as shock wave lithotripsy (SWL) and histotripsy directly rely on cavitation. In SWL, the erosive effect of collapsing bubbles contributes to fractionation of kidney stones (Bailey et al. 2003). Histotripsy is a non-invasive focused ultrasound procedure that uses cavitation generated by highamplitude ultrasound pulses to mechanically destroy soft tissue (Parsons et al. 2006; Roberts et al. 2006; Xu et al. 2005). Experimental studies of histotripsy-induced cavitation in tissue phantoms and animal models have illustrated the influence of tissue mechanical properties (Vlaisavljevich et al. 2014, 2015b) and bubble growth (Vlaisavljevich et al. 2015c). At present, however, the mechanisms responsible for tissue damage observed in histotripsy and other cavitation-inducing ultrasound treatments remain difficult to quantify. There is strong evidence that stiffer tissues are more resistant to cavitation damage. However, the mechanics of cell-bubble interactions and the influence of material properties, for example, shear modulus, viscosity and ultimate stress/ strain, are less clear (Vlaisavljevich et al. 2013). An improved understanding of cavitation-induced tissue damage mechanisms will facilitate the development of effective means of planning and monitoring therapeutic ultrasound procedures, as well as improve the treatment's tolerability and efficacy (Miller et al. 2012). Understanding the influence of tissue properties on damage could enable optimization of treatment parameters for different tissues, which would be particularly important for the development of self-limiting and vessel-sparing clinical applications (Vlaisavljevich et al. 2013).

such as elasticity on the cavitation threshold

Multiple mechanisms for cavitation-induced damage during ultrasound procedures have been proposed,

Conflict-of-interest disclosure: E.V. and Z.X. have financial interests and/or other relationship with HistoSonics Inc.

Address correspondence to: Lauren Mancia, 1231 Beal Avenue, Ann Arbor, MI 48109-2133, USA. E-mail: lamancha@umich.edu Conflict-of-interest disclosure: E.V. and Z.X. have financial inter-

including shock waves and high temperatures at bubble collapse, as well as re-entrant jets produced during aspherical bubble collapse (Nyborg et al. 2002). Experimental observations (De et al. 2007; Vlaisavljevich et al. 2016a) indicate that local deformations in the vicinity of histotripsy bubbles can be considerable, occur rapidly and depend on the material properties. It is thus reasonable to hypothesize that cavitationinduced mechanical loading is a potential tissue damage mechanism in histotripsy. Correlations between high tensile strength and resistance to tissue damage also suggest that stress, in particular, contributes to tissue rupture in histotripsy (Vlaisavljevich et al. 2013). However, experimental measurements of local, highly transient, cavitation-induced stresses and strains are difficult to obtain because of limited spatiotemporal resolution and optical access (Zimberlin et al. 2007). To bypass these challenges, spherical bubble dynamics are numerically modeled in a soft material (Warnez and Johnsen 2015), thus quantifying localized stress and strain distributions in simulated tissues exposed to histotripsy pulses.

Deformations produced in viscoelastic media by single cavitation bubbles exposed to harmonic forcing have been computed previously (Church and Yang 2006). The current study is unique in providing independent consideration of different tissue mechanical properties and waveform characteristics on several proposed damage mechanisms (stresses, finite strains and strain rates) developed during cavitation under histotripsy forcing. Stress and strain fields are considered in different reference frames to facilitate experimental comparisons. The focus is to quantify proposed damage mechanisms to identify specific contributors to tissue damage and to provide a theoretical basis for the development and enhancement of damage metrics. Furthermore, recent experimental investigations of cells (neurons) exposed to large compressive strains at high rates revealed that a critical strain threshold must be met to produce cell death, but that the extent of cell death depends on strain rate (Bar-Kochba et al. 2016). The present work presents a means of identifying the relative influence of strain (dominated by tissue elasticity) versus strain rate (proportional to tissue viscosity) as a function of distance from the bubble wall, which could provide a more detailed prediction of lesion morphology in different tissue types.

The numerical methods in this study were previously used to complement experimental investigations of histotripsy-induced cavitation thresholds (Vlaisavljevich et al. 2014, 2015b, 2016b), bubble growth (Vlaisavljevich et al. 2015c) and cell-bubble interactions (Vlaisavljevich et al. 2016a). After description of the theoretical model and problem setup, methods for calculating field quantities are introduced. Next, the results of a simulation parameter study are provided to

illustrate the influence of tissue (viscosity, shear modulus, nucleus size) and waveform (amplitude, frequency) properties on stress and strain developed in the tissue. Finally, a relationship is identified between the dominant contribution to viscous versus elastic stress and distance from the bubble nucleus.

THEORETICAL MODEL

Early theoretical models were developed to study bubbles driven hydrodynamically (Plesset 1949) and acoustically (Noltingk and Neppiras 1950) in liquids. More recently, non-Newtonian models have been used to investigate cavitation in viscoelastic materials representative of polymer gels (Shima and Tsujino 1982) and soft biological tissue (Brujan 2010). Several constitutive models have been adapted to the study of cavitation with the intention of mimicking the dynamics of bubbles in soft tissue, including the Maxwell (Allen and Roy 2000a), Kelvin-Voigt (Yang and Church 2005), Oldroyd (Allen and Roy 2000b) and Zener (Hua and Johnsen 2013) models. The present study simulates the dynamics of a single, spherical bubble in a compressible Kelvin-Voigt-based viscoelastic solid with non-linear elasticity (Gaudron et al. 2015), which accounts for the reference configuration of the tissue. Our model includes a hyperelastic term derived from finite-strain theory to adequately represent the large deformations encountered in the nanometer- to micron-scale bubble growth observed in histotripsy.

This study considers a spherical, homobaric bubble in an infinite, homogenous viscoelastic medium. To account for acoustic radiation losses, the bubble dynamics are described by the equation of Keller and Miksis (1980)

$$\left(1 - \frac{\dot{R}}{c_{\infty}}\right) R \dot{R} + \frac{3}{2} \left(1 - \frac{\dot{R}}{3c_{\infty}}\right) \dot{R}^{2} = \frac{1}{\rho_{\infty}} \left(1 + \frac{\dot{R}}{c_{\infty}} + \frac{R}{c_{\infty}} \frac{d}{dt}\right) \times \left[p_{\rm B} - \left(p_{\infty} + p_{\rm f}\left(t + \frac{R}{c_{\infty}}\right)\right) - \frac{2S}{R} + J\right], \tag{1}$$

where R is the bubble radius, c_{∞} and ρ_{∞} are the constant sound speed and density of the medium and S is the surface tension. The far-field pressure is the sum of the ambient pressure, p_{∞} , and time-varying ultrasound forcing, $p_{\rm f}(t)$ (eqn [8]). The pressure of the non-condensable air inside the bubble is given by the polytropic relationship $p_{\rm B} = p_0(R_0/R)^{3\kappa}$, where $p_0 = p_{\infty} + 2S/R_0$ is the pressure inside the bubble at equilibrium. Gas inside the bubble is assumed to behave isothermally with a polytropic coefficient $\kappa = 1$, which is expected to be an accurate representation of the heat transfer. For simplicity, the tissue—bubble boundary is assumed to be impervious to gas, and vapor inside the bubble is neglected. These assumptions could potentially underpredict the bubble

size (Harvey et al. 1944); however, this error is expected to be minor because the mass boundary layer thickness is small relative to the bubble radius throughout bubble expansion (Barajas and Johnsen 2017). The integral of deviatoric stresses in the surrounding tissue is

$$J = 2 \int_{R}^{\infty} \frac{\tau_{rr} - \tau_{\theta\theta}}{r} dr \tag{2}$$

where r is the radial distance from the origin, and $\tau_{rr} \tau_{\theta\theta}$ are the radial and polar stress components, respectively.

Constitutive model

A Kelvin–Voigt-based constitutive model relates the deviatoric stress, τ , and strain, \mathbf{E} , tensors in the surrounding tissue whose coordinates span $r \in [R,L]$, where L is the arbitrary size of the domain. In this formulation, the stress at any field coordinate r in the surroundings is the sum of viscous and elastic contributions,

$$\tau_{rr} = \tau_{rr}^{V} + \tau_{rr}^{E}$$

$$= -4\mu \frac{R^{2} \dot{R}}{r^{3}} + \frac{2G}{3} \left[\left(\frac{r_{0}}{r} \right)^{4} - \left(\frac{r}{r_{0}} \right)^{2} \right]$$
(3)

where μ is the viscosity, G is the (linear) shear modulus and the original and current radial coordinates are related via

$$r_0(r,t) = \sqrt[3]{r^3 - R^3 + R_0^3} \tag{4}$$

For an incompressible near field with spherical symmetry, $\tau_{\theta\theta} = -\tau_{rr}/2 = \tau_{\varphi\varphi}$. By convention, a negative stress at any point in the surroundings represents compression of the corresponding material element, and a positive stress represents tension ("stretching"). Figure 1 is a schematic of the radial stresses and strains on a wedge of tissue during bubble growth and bubble collapse. The shape of the wedge changes as the bubble deforms the surrounding medium, but its mass and volume are conserved. Derived using continuum mechanics formalism, this model ensures that finite deformations $r(r_0,t)$ about the original configuration r_0 are accurately represented during bubble oscillations. Figure 2 illustrates the configuration of the bubble and surrounding medium before and after deformation. Labeled coordinates correspond to the variables related by eqns (3) and (4). Evaluating eqn (3) at the bubble wall yields the following constitutive expression in the Keller-Miksis equation:

$$J = -\frac{4\mu\dot{R}}{R} - \frac{G}{2} \left[5 - 4\left(\frac{R_0}{R}\right) - \left(\frac{R_0}{R}\right)^4 \right]$$
 (5)

Strain fields in the surrounding tissue are computed using the Hencky (or true) strain definition

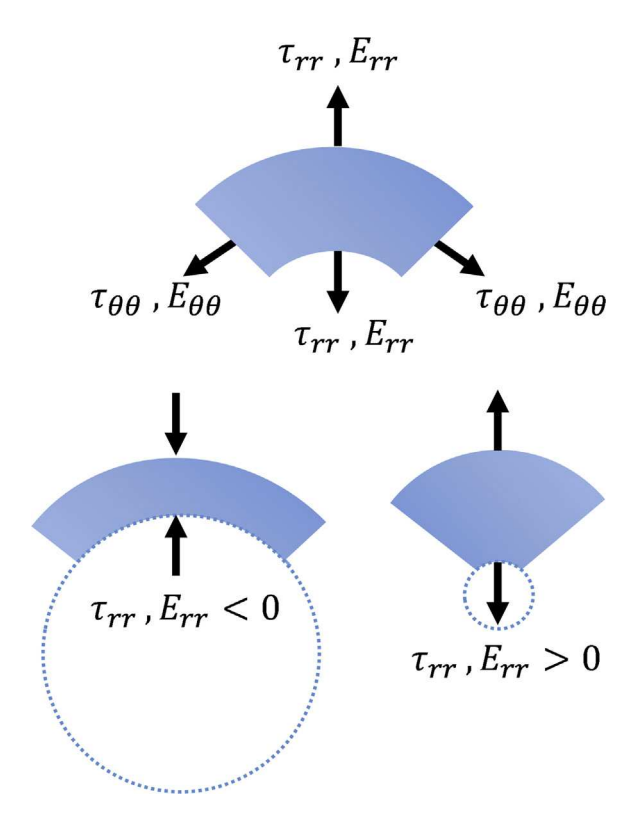


Fig. 1. Radial (τ_{rr}) and polar $(\tau_{\theta\theta} = -\tau_{rr}/2 = \tau_{\varphi\varphi})$ stresses and strains on a wedge of tissue during bubble growth (left) and collapse (right).

$$E_{rr}(r,t) = \frac{2}{3} \log \left(1 - \frac{R^3 - R_0^3}{r^3} \right)$$

$$E_{\theta\theta}(r,t) = -\frac{1}{3} \log \left(1 - \frac{R^3 - R_0^3}{r^3} \right)$$
(6)

to describe tissue deformation in successive increments of classical engineering strain (Xiao 2005), and the strain corresponds to the summation of incremental increases in displacement divided by length in the current configuration. The true strain definition is chosen because it most closely approximates the smooth increases in strain observed in experimental studies of cell-bubble interactions (Vlaisavljevich et al. 2016a). This definition has

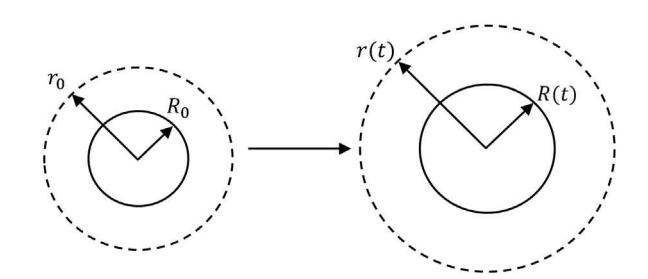


Fig. 2. Schematic illustrating bubble radius and material coordinates in undeformed and deformed configurations.

also been favored for measurements of vascular tissue properties because it provides a more direct measure of a material's instantaneous response to applied stress (Khanafer et al. 2013). Strain rates are calculated by taking the material derivative of the strain, where $u_r = R^2 R / r^2$ is the radial velocity component:

$$\frac{DE_{rr}}{Dt} = \frac{\partial E_{rr}}{\partial t} + u_r \frac{\partial E_{rr}}{\partial r} = -2 \frac{R^2 \dot{R}}{r^3}$$

$$\frac{DE_{\theta\theta}}{Dt} = \frac{\partial E_{\theta\theta}}{\partial t} + u_r \frac{\partial E_{\theta\theta}}{\partial r} = \frac{R^2 \dot{R}}{r^3}$$
(7)

Like the stresses, the radial and polar strains differ by a factor of -2, as do the corresponding strain rates.

Problem setup

Viscoelastic parameters within the range of values previously studied in histotripsy experiments in tissues (Diamond 1999; Duck 2013; Maxwell et al. 2013; Wells and Merrill 1962) and tissue phantoms (Vlaisavljevich et al. 2015b, 2015c) are considered: $\mu = 1$ –100 mPa·s, G = 1–1000 kPa. Other tissue parameters are fixed: kg/m³, S = 72 mN·m and $c_{\infty} = 1497$ m/s, corresponding to values in water at 25°C. As in our past studies (Vlaisavljevich et al. 2014, 2015b, 2015c, 2016a, 2016b), the growth of a pre-existing gas nucleus is initiated by a single negative histotripsy cycle:

$$p_{\rm f}(t) = \begin{cases} p_{\rm A} \left(\frac{1 + \cos[\omega(t - \delta)]}{2} \right)^n, & \left| t - \delta \right| \le \frac{\pi}{\omega}, \\ 0, & \left| t - \delta \right| > \frac{\pi}{\omega}. \end{cases}$$
(8)

This work investigates the dependence of the bubble dynamics on the pressure amplitude $p_{\rm A}=20$ –60 MPa and "frequency" $\omega=0.5$ –5 MHz corresponding to this single

cycle; the time delay is $\delta = 5 \mu s$, and n = 3.7 is a fitting parameter chosen to match the shape and duration of a typical histotripsy cycle.

Using the characteristic velocity $u = \sqrt{p_{\infty}/\rho_{\infty}}$, density and the initial radius for non-dimensionalization, the following dimensionless parameters govern the problem: Reynolds $(\rho_{\infty}uR_0/\mu)$, Weber $(\rho_{\infty}u^2R_0/S)$, Cauchy $(\rho_{\infty}u^2/G)$ and Mach (u/c_{∞}) numbers, as well as the polytropic index κ , dimensionless amplitude p_A/p_{∞} and frequency $\omega R_0/u$. As in our past studies, the resulting dimensionless system of differential equations is numerically integrated using the MATLAB stiff ODE solver ode15s (The Math-Works, Natick, MA, USA) (Shampine and Reichelt 1997). Our subsequent parametric study will consider the effects of varying μ , G, p_A , ω and R_0 .

RESULTS: BASELINE CASE

Our baseline case consists of a tissue with $\mu = 15$ mPa·s and G = 2.5 kPa, initial nucleus size $R_0 = 5$ nm based on experimentally inferred nucleus sizes (Maxwell et al. 2013; Vlaisavljevich et al. 2015a) and waveform with amplitude $p_A = -30$ MPa and frequency $\omega = 1$ MHz. This baseline is chosen because it is within the parameter range of our previous studies (Vlaisavljevich et al. 2014, 2015b, 2015c, 2016a, 2016b) and illustrates a transition from strain-dominated to strain rate-dominated mechanical effects. Figure 3 illustrates the time history of the bubble radius and driving pressure. The large peak negative pressure of the histotripsy pulse causes a large expansion phase to a maximum radius of 200 µm, followed by a violent collapse to a minimum radius < 5 nm, which dissipates the energy primarily via compressibility. A single, low-amplitude rebound back to initial bubble radius is resolved, though not evident on the scale of this plot. A detailed study of minimum bubble

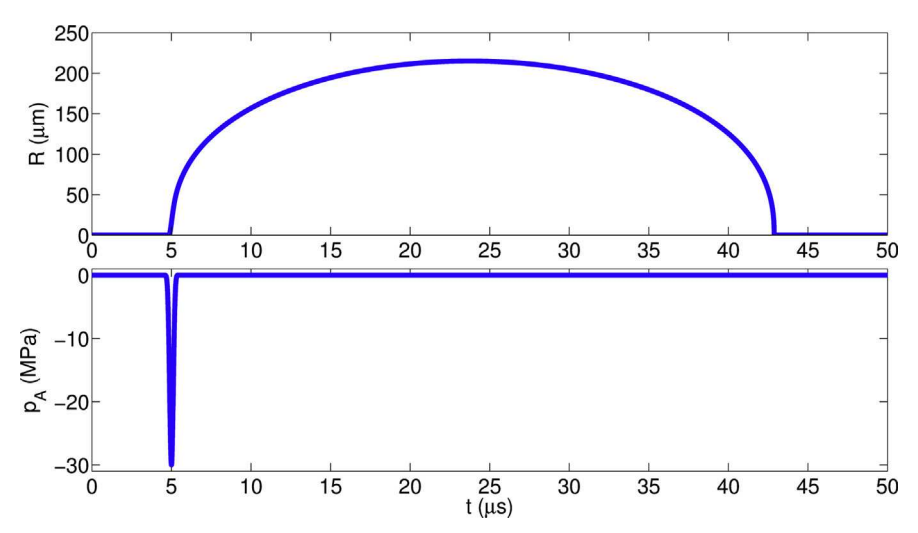


Fig. 3. Time history of the bubble radius (top) driven by a single negative histotripsy cycle (bottom) for the baseline case.

radius lies beyond the scope of this study as histotripsy bubbles display more complex behavior at collapse, such as breakup (Duryea et al. 2015); the present focus is on the dynamics until just before collapse.

Spatiotemporal evolution of the total radial stress in the tissue is illustrated in Figure 4. In addition to the color maps, the time evolution of stresses along Lagrangian trajectories starting at different initial distances from the bubble wall and the radial stress distributions at fixed times are included. The tissue experiences large negative stresses near the bubble wall at the start of growth as the tissue is radially compressed. The highest stresses occur when the bubble reaches its maximum radius and the surrounding tissue is under maximal compression. The total radial stress is not symmetric in time about the maximum radius, illustrated by the large tensile (positive) stresses at collapse as the shrinking bubble releases the compressed tissue to

assume its original configuration. Stress magnitudes are greatest near the bubble wall and rapidly attenuate farther into the medium such that they are negligible within 200 μ m from the bubble wall. The stresses persisting deeper in the tissue are small (<0.01 MPa), compared with those within 1 μ m of the bubble wall, which can exceed 100 MPa. The highest stresses are so localized to the bubble wall that they are better appreciated in the Lagrangian trajectories, where the spherical coordinate system moves with the tissue as it deforms over time. The stresses are computed from eqn (3) along trajectories r(t) for particles starting at different initial locations, r_0 , in eqn (4). Such a particle could, for instance, represent a cell, whose stress one is interested in monitoring. As the bubble grows and collapses, the Lagrangian points oscillate with the surroundings. By mass conservation, the distance between the Lagrangian trajectories decreases when the

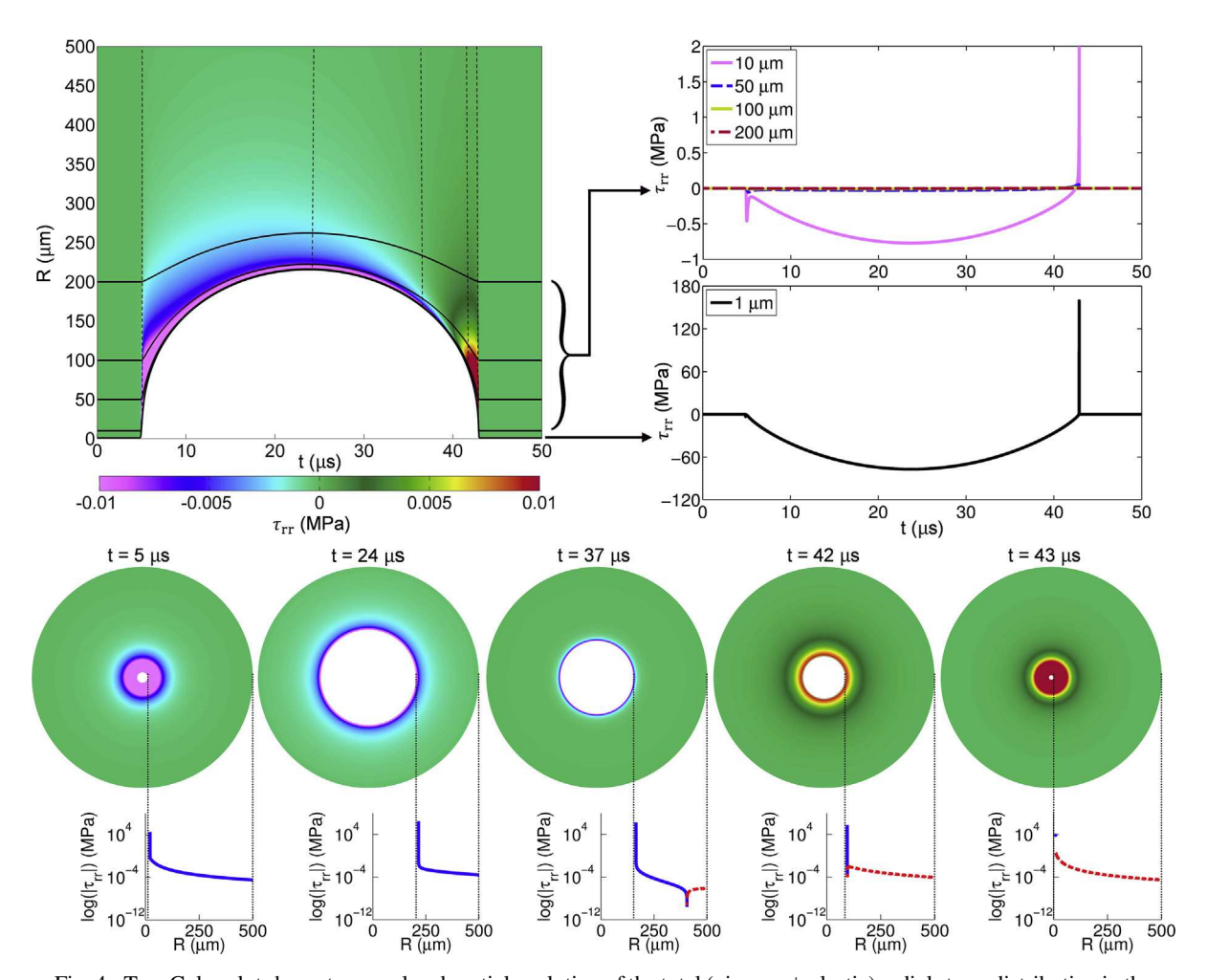


Fig. 4. Top: Color plot shows temporal and spatial evolution of the total (viscous + elastic) radial stress distribution in the tissue for the baseline case. *Solid lines* correspond to stresses experienced as a function of time along Lagrangian trajectories starting 1 to 200 μm from the bubble nucleus, with stress magnitude along each trajectory indicated by arrows at right. *Vertical dashed lines* correspond to stresses in the surroundings at fixed times given below. Bottom: "Bubble" color plots show stresses at fixed times between 5 and 41 μs, with traces indicating the magnitudes of compressive stresses (*solid blue*) and tensile stresses (*dashed red*) as a function of distance from the bubble wall.

bubble grows, and vice versa during collapse. A particle in the tissue starting 1 μ m from the bubble nucleus experiences smoothly increasing compressive stress in the radial direction, with a maximum compressive stress of -77MPa at maximum radius. A nearly instantaneous peak in tensile stress of 160 MPa occurs at minimum radius. For particles starting 10–50 μ m from the bubble wall, the compressive stress at maximum radius and the tensile stress at collapse are significantly attenuated. The stress profile for a particle starting 10 μ m from the bubble wall exhibits a peak in compressive stress at the onset of growth also present but not clearly visible in the 1-µm trace because of early explosive growth. Further growth is restricted by tissue stiffness, and slowed subsequent growth produces a smoothly increasing compressive stress in surroundings. As in the 1- μ m case, particles initially 10 µm from the bubble nucleus experience a nearinstantaneous peak in tensile stress at collapse; however, the magnitude of maximum tensile stress is reduced to 2 MPa at the greater distances. Particles starting 50-200 µm from the bubble nucleus also experience decreasing stress magnitudes. At 50 μ m from the bubble wall, the instantaneous peak tensile stress at collapse has largely attenuated and reaches 0.052 MPa, whereas the compressive stress at maximum radius is -0.057 MPa. There is a further dramatic decrease in stress magnitude experienced by cells 200 μ m from the nucleus. Considering that most ruptured tissues have an ultimate tensile strength > 0.05 MPa (Vlaisavljevich et al. 2013), an order of magnitude comparison suggests that radial tensile stress capable of rupturing most tissues is confined to a radius of approximately 50 μ m surrounding a nucleation site, a finding consistent with observations of sharp lesion boundaries in previous experimental studies of histotripsy (Roberts et al. 2006).

The susceptibility of tissue to histotripsy-induced damage depends on the tissue's mechanical properties (Vlaisavljevich et al. 2013), and the stress in a viscoelastic tissue depends on strain and strain rate. However, the influence of individual tissue properties on susceptibility to damage is less clear. Thus, separating the stress into its viscous and elastic components is useful for

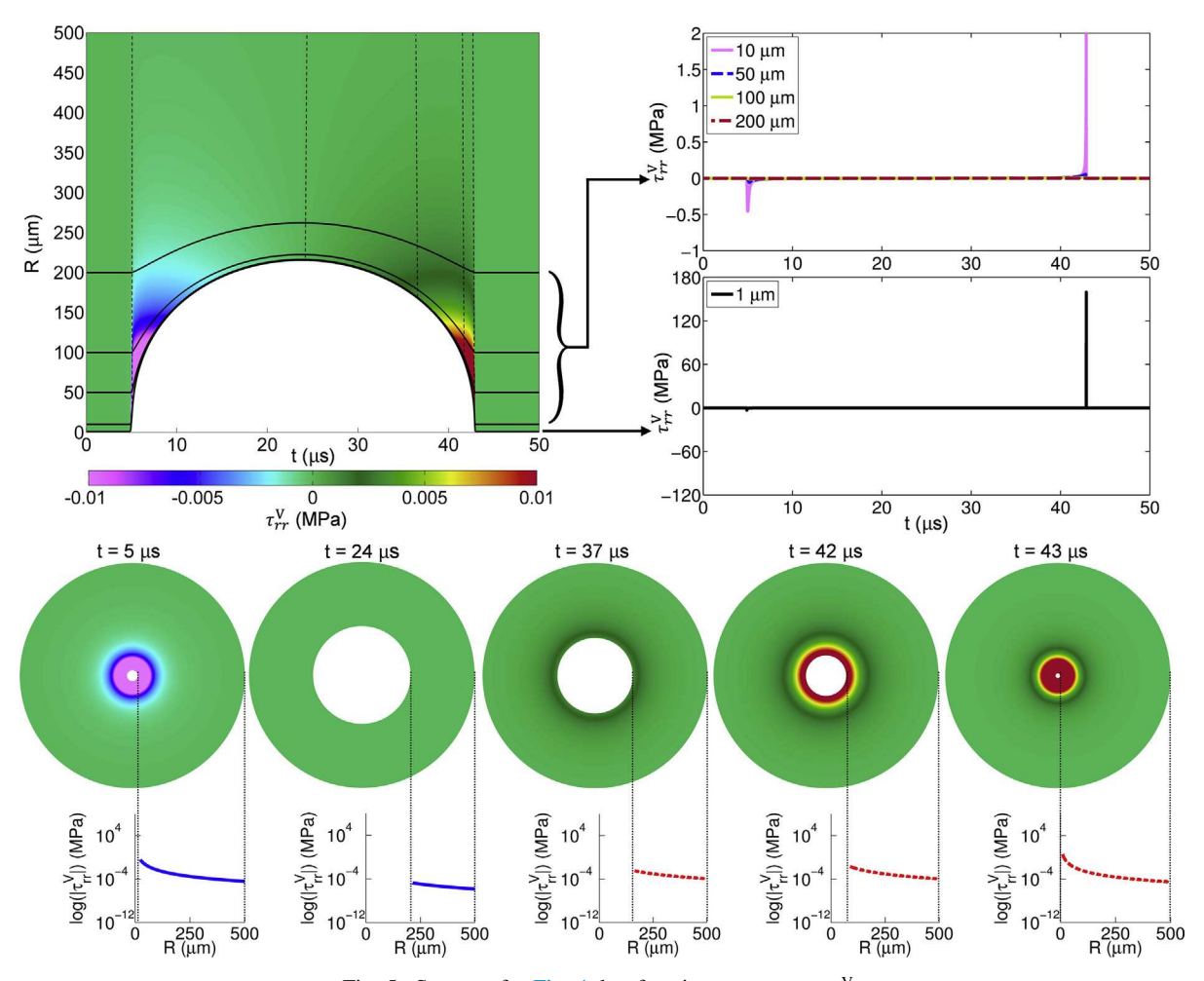


Fig. 5. Same as for Fig. 4, but for viscous stresses, τ_{rr}^{V} .

postulating how potential stress-related damage mechanisms depend on tissue properties. The time evolution of the viscous and elastic radial stress distributions in the tissue for the baseline case is illustrated in Figures 5 and 6, respectively. Viewing each component separately indicates that the extrema observed in the total radial stress field originate from different mechanisms. The sharp instantaneous peaks in total stress at early growth and late collapse are due to viscous contributions. Viscous stresses dissipate the kinetic energy of the surroundings into heat as

$$\phi = \underline{\boldsymbol{\tau}} : \nabla \boldsymbol{u} = 12\mu \left(\frac{R^2 \dot{R}}{r^3}\right)^2 = -3\frac{R^2 \dot{R}}{r^3} \tau_{rr}^V \tag{9}$$

Dissipation increases with increasing tissue viscosity, which in turn limits bubble growth and decreases the velocity of the bubble wall just before collapse. Because viscous stresses at the bubble wall are proportional to \dot{R}/R , the stress is compressive (negative) at early growth and tensile at collapse (positive). Otherwise,

viscous stresses are negligible. The more gradually increasing stresses at maximum radius are purely elastic and are only compressive because the bubble does not reach a radius much smaller than its initial value of 5 nm.

The stresses correspond to different deformation modes: as evidenced by eqn (3), elastic stresses are proportional to strains (deformation from the initial configuration), whereas viscous stresses are proportional to strain rates (velocity differentials). Strains and the corresponding rates are quantities that can be measured in experiments without a priori knowledge of the constitutive model that describes a particular tissue. Figure 7 illustrates the temporal evolution of Hencky radial strains based on Lagrangian and Eulerian (calculated with respect to a fixed coordinate system) viewpoints. The seemingly larger values in the Lagrangian viewpoint are due to the diverging geometrical field during bubble growth: by conservation of mass, particles starting at a given distance from the bubble end up closer to the bubble wall during expansion. Both plots indicate that strains remain concentrated near the bubble wall and attenuate

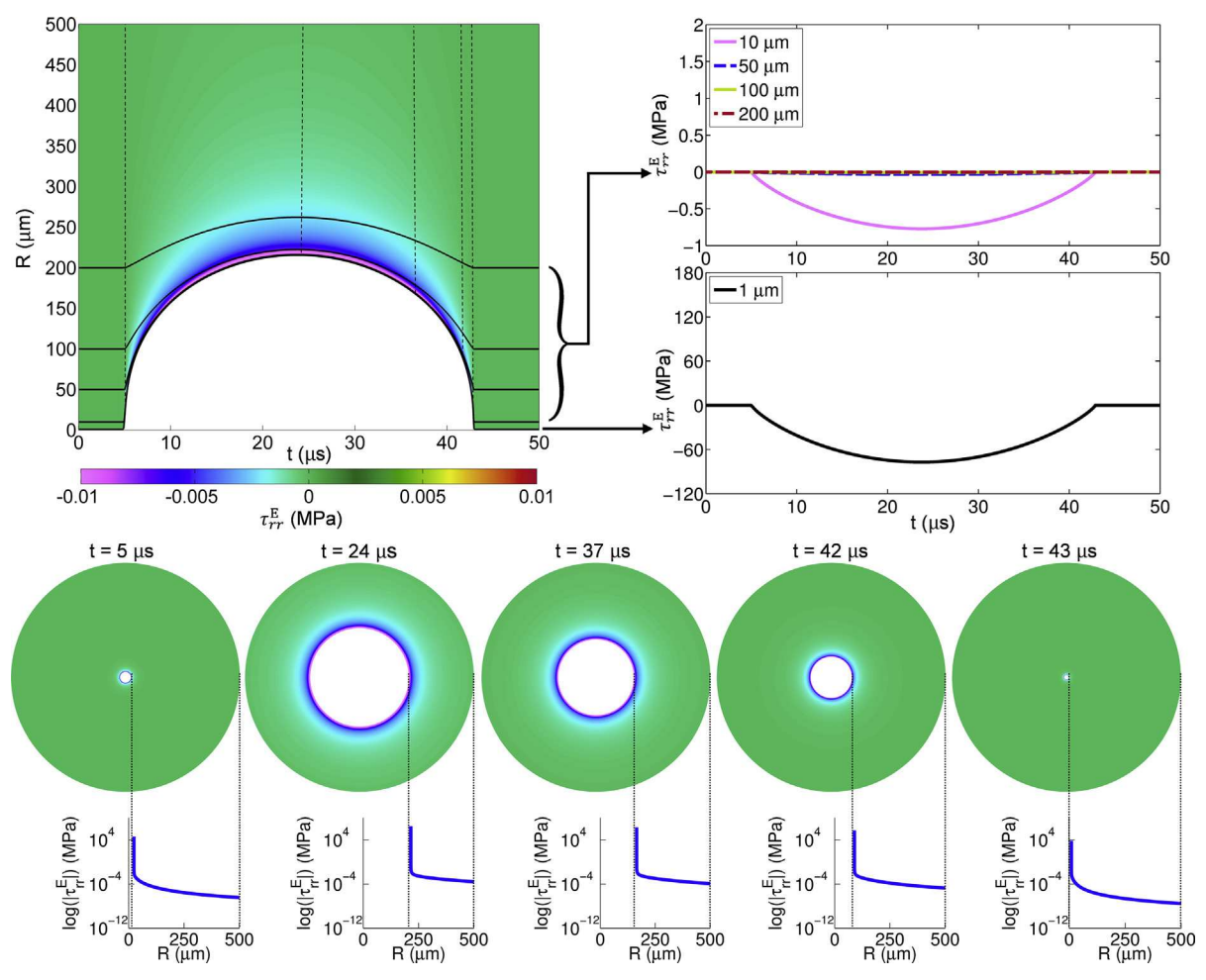


Fig. 6. Same as for Fig. 4, but for elastic stresses, $\tau_{rr}^{\rm E}$

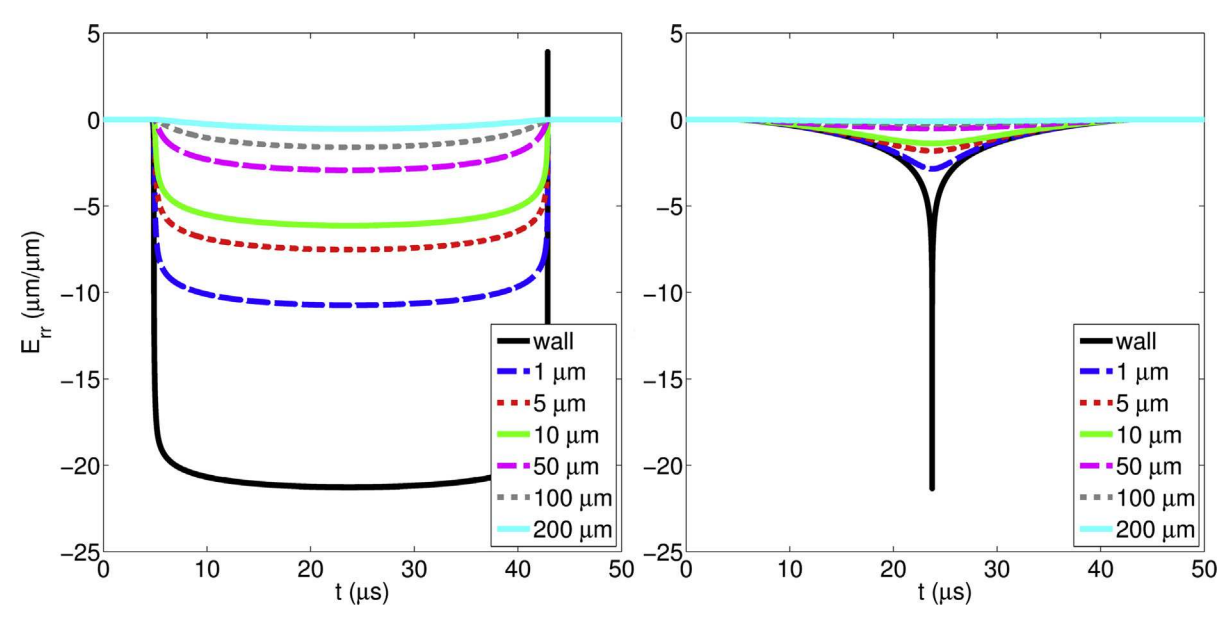


Fig. 7. Radial strains versus time following Lagrangian trajectories (left) and at Eulerian points (right). Distances correspond to the different initial distances of the particles from the origin (Lagrangian) and to the initial distances from the maximum radius (Eulerian).

rapidly with increasing depth into the surrounding tissue. Large radial strains that persist to greater depths in the tissue are compressive and occur when maximum bubble radius is reached. Lagrangian particles experience radial compressive strains that smoothly increase to a maximum at maximum radius. Eulerian strains progressively increase as maximum radius is reached, but are less than $1.0 \,\mu\text{m}/\mu\text{m}$ until the bubble radius reaches approximately 150 μ m. As the bubble reaches its maximum radius (and approaches the position of the fixed Eulerian point), the strains achieve a maximum and then decrease rapidly with distance from that point. Strain magnitude varies significantly with distance from the bubble in each depiction. In the Lagrangian depiction, radial compressive strains experienced by particles starting within 50 μ m from the nucleus are high, for example, $-11 \mu m/\mu m$ starting at 1 µm from the nucleus wall. Radial compressive strain experienced by particles starting 200 μ m from the nucleus is significantly lower at $-0.54 \mu \text{m}$ / μm. In the Eulerian depiction, maximum compressive stresses achieve the same value of $-21 \mu m/\mu m$ at the bubble wall at maximum radius, but maximum compressive strains are $-2.9 \mu \text{m}/\mu \text{m}$ at $1 \mu \text{m}$ and $-0.10 \mu \text{m}/\mu \text{m}$ at 200 μ m from the maximum bubble radius. For comparison, tissue measurements suggest that the ultimate fractional tensile strain of tissues ruptured by histotripsy ranges from 0.43 μ m/ μ m for small intestine to 1.5 μ m/ μ m for uterine wall (Vlaisavljevich et al. 2013).

The largest strains are experienced by particles starting at the bubble wall when the bubble reaches its maximum and minimum radii; exact expressions for the maximum radial compressive, polar tensile, radial

tensile and polar compressive strains are summarized in Table 1. First, when the bubble achieves its maximum radius, radial strain at the bubble wall is compressive and polar strain at the bubble wall is tensile, corresponding to the maximum radial compressive and polar tensile stresses. In contrast, the largest radial tensile and polar compressive strains occur when the bubble collapses to its minimum radius, $R_{\min} < R_0$. At this instant, the tissue is fully released from the compressive radial strain that occurred during bubble growth, and the strain changes direction. These strains occur over an exceedingly short time and attenuate much more rapidly into surrounding tissue than the strains generated at maximum bubble radius. As seen in Figure 7, Lagrangian particles starting as close as 1 µm from the bubble nucleus experience negligible radial tensile strain at bubble collapse. The highest strain rates occur at instants of initial bubble growth and late collapse, with maximum values ranging from 10⁵ s⁻¹ for a Lagrangian particle starting at a distance of 200 μm from the bubble wall to 10^8 s⁻¹ at a distance of 1 μ m

Table 1. Magnitude of maximum strain experienced by a particle starting at the wall of the bubble nucleus*

Location	Direction	Deformation	Expression
Maximum radius	Radial	Compression	$E_{rr}(R_{\text{max}}) \rightarrow 2\log(R_{\text{max}}/R_0)$
	Polar	Tension	$E_{\theta\theta}(R_{\text{max}}) \rightarrow \log(R_{\text{max}}/R_0)$
Minimum radius	Radial	Tension	$E_{rr}(R_{\min}) \rightarrow 2\log(R_0/R_{\min})$
	Polar	Compression	$E_{\theta\theta}(R_{\min}) \rightarrow \log(R_0/R_{\min})$

^{*} Absolute maximum strains occur when the bubble reaches its maximum radius, and relative maximum strains occur at minimum bubble radius.

from the bubble wall. The highest strain rates coincide with the peaks in radial tensile stress and strain that occur at the bubble wall at R_{\min} .

RESULTS: PARAMETRIC STUDY

The effects of tissue (viscosity, shear modulus) and waveform (negative pressure, frequency) properties, as well as initial bubble radius, on maximum radial stresses and strains experienced by a Lagrangian particle (e.g., a cell) are evaluated. The Lagrangian viewpoint is of practical relevance because it enables one to determine the loads experienced by a cell, initially at some distance from the nucleation site, over the course of bubble growth and collapse. In all of the following maximum stress (Figs. 9, 12, 15, 18, 21) and strain (Figs. 10, 13, 16, 19, 22) figures, the horizontal axis gives the starting point of a particle within 50 μ m from the bubble nucleus, with 500 sample points. The vertical axis has the highest magnitude of total stress (combined elastic and viscous) or strain experienced by a cell that starts at a given distance from the nucleus. Because of their typically distinct origins, maximum compressive and tensile stresses are considered separately. As a reference, a water case in which viscosity and shear modulus are fixed at $\mu = 1$ mPa·s and G = 0 Pa is used when tissue material properties are varied. Results are provided for radial stresses and strains; tissue is also experiencing polar stresses and strains, of opposite sign and half the magnitude.

Viscosity

Figures 8, 9 and 10 illustrate the time history of the bubble radius, maximum radial compressive/tensile stress and maximum radial compressible (Hencky) strain experienced by Lagrangian particles starting at different distances from the bubble for $\mu = 1$, 5, 15, 50 and 100 mPa·s, fixing shear modulus (G = 2.5 kPa) and other parameters at their baseline values. Equivalently, this corresponds to varying the Reynolds number while holding all other dimensionless parameters fixed.

Increased viscous resistance impedes bubble growth, as evidenced by the reduction in the maximum bubble radius at higher viscosities. As the viscosity is increased, the collapse phase (from R_{max} to R_{min}) becomes longer than the growth phase (from a stationary nucleus of radius R_0 to R_{max}). This asymmetry originates from the dissipative nature of viscous effects. For a given viscosity, the maximum tensile stress (produced at collapse) smoothly and monotonically decreases with initial distance. However, slightly lower tensile stress is achieved in the 100 mPa·s medium than in the 50 mPa·s medium. This behavior is again due to increased viscous dissipation, which gives rise to lower velocities at collapse and, thus, smaller tensile stresses. At sufficiently high viscosities, the maximum compressive stress exhibits a "kink"—a discontinuous slope—highlighted in Figure 9 with an inset and subsequently with open circles. This point corresponds to the initial distance of the "cell" from the origin at which the absolute maximum compressive stress transitions from elastic to viscous over the course of the simulation. The absolute maximum compressive stress is of elastic origin and occurs at the bubble wall when the bubble reaches its maximum radius. As initial distance into the tissue is increased, this elastic stress decreases according to the second term in eqn (3). In contrast, a maximum in viscous compressive stress occurs at the bubble wall when growth is initiated; the viscous compressive stress decreases according to the first term in eqn (3). Increasing viscosity enhances the importance of viscous stresses relative to their elastic counterparts in two important ways: the coefficient weighing viscous contributions (μ) is increased compared with that weighing elastic contributions (G), and the maximum radius is reduced. As a result, the attenuation of elastic stresses for particles starting farther away from the bubble is greater than that for viscous stresses. At larger viscosities (15-100 mPa·s), viscous stresses at the onset of bubble growth exceed elastic stresses (at maximum bubble radius) closer to the bubble wall. As a reflection of decreasing maximum bubble radius with increasing viscosity, compressive strain consistently

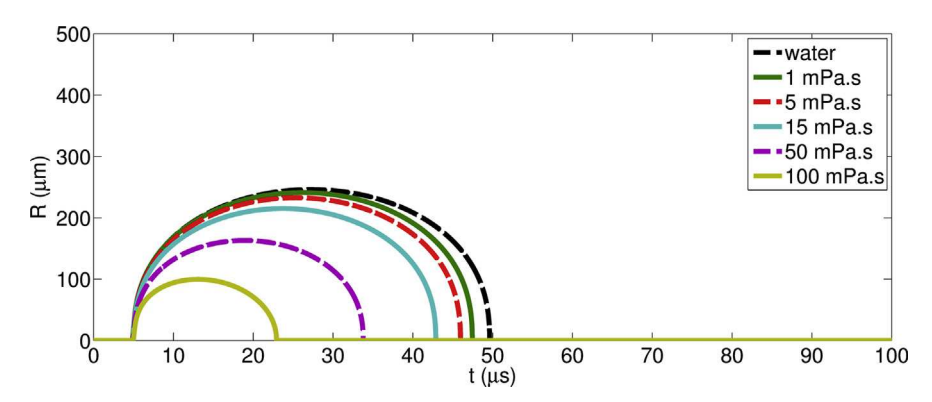


Fig. 8. Time history of bubble radius for media of different viscosities ($\mu = 1, 5, 15, 50$ and 100 mPa·s).

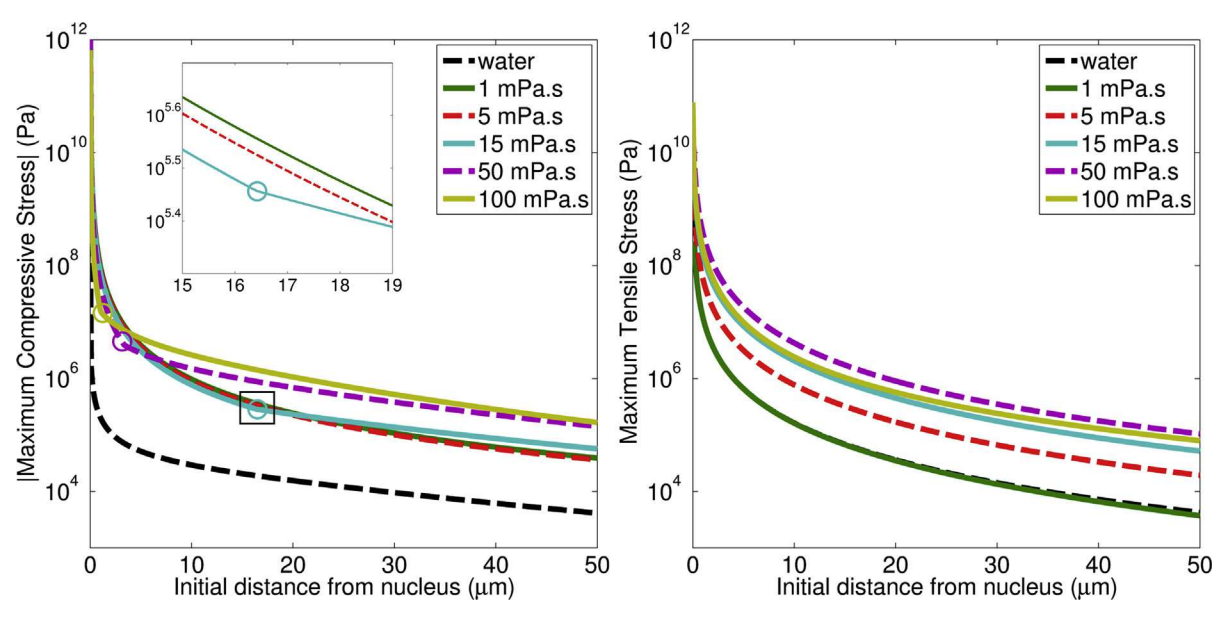


Fig. 9. Maximum compressive (left) and tensile (right) stresses versus initial distance from the bubble nucleus in media of different viscosities ($\mu = 1, 5, 15, 50$ and $100 \text{ mPa} \cdot \text{s}$). The elastic-to-viscous transitions are circled on the compressive stress traces.

decreases. Media with viscosities between 1 and 15 mPa·s (including water), exhibit similar maximum bubble radii and, hence, compressive strains of similar magnitude.

Shear modulus

Figures 11, 12 and 13 illustrate the time history of the bubble radius, maximum radial compressive/tensile stress and maximum radial compressible (Hencky)

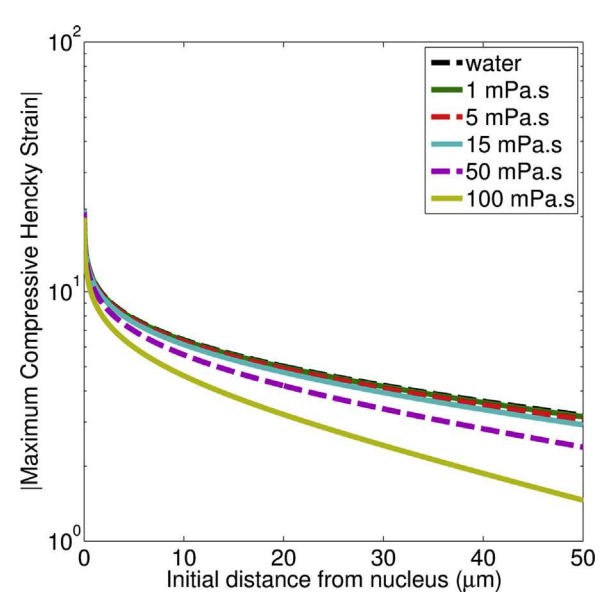


Fig. 10. Maximum compressive Hencky strain versus distance from the bubble nucleus in media of different viscosities $(\mu = 1, 5, 15, 50 \text{ and } 100 \text{ mPa} \cdot \text{s}).$

strain experienced by Lagrangian particles starting at different distances away from the bubble for G=0,1,2.5,10,100 and 1000 kPa, fixing viscosity ($\mu=15$ mPa·s) and other parameters at their baseline values. Equivalently, this corresponds to varying the Cauchy number while holding all other dimensionless parameters fixed.

Increased tissue stiffness reduces bubble growth, as evidenced by the smaller maximum radii and shorter collapse time (from R_{max} to R_{min}) achieved at higher shear modulus. Contrary to viscosity, elasticity is a restoring force with no direct dissipative effects. Symmetry between growth and collapse phases is thus not affected by elasticity. The dominance of elastic stress close to the bubble wall is evident when cases of non-zero shear moduli are compared with water. The maximum compressive stress increases with increasing shear modulus, whereas the maximum tensile stress and compressive strain decrease with increasing modulus. As in the previous section, a "kink" is observed in the G = 1 kPa and G = 2.5 kPa traces for maximum compressive stress, marking the locations at which the dominant stress contribution changes from elastic to viscous. Decreasing the shear modulus reduces the relative importance of elastic contributions compared with viscous stresses. The maximum tensile stress experienced by particles in the tissue exhibits only limited dependence on the shear modulus for G < 100 kPa, which is expected because this quantity strongly depends on viscous stresses and because the bubble radius histories are similar. For larger G, smaller maximum tensile stresses are achieved. Again, differences

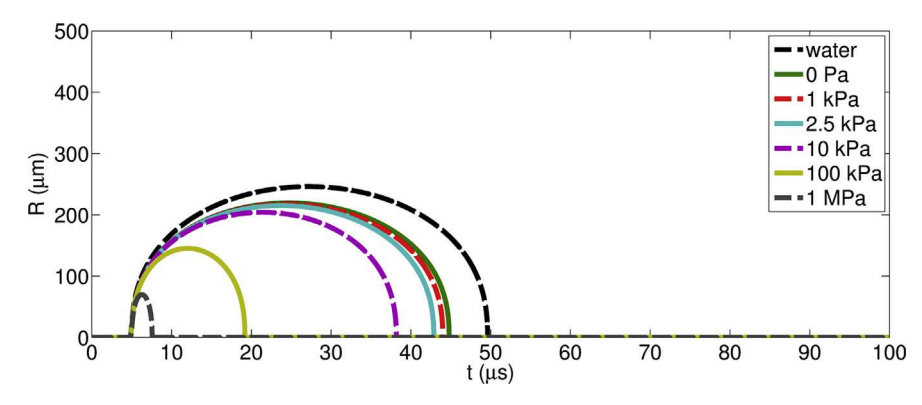


Fig. 11. Time history of bubble radius for media of different shear moduli (G = 0, 1, 2.5, 10, 100 and 1000 kPa).

in compressive strain developed at all distances from the bubble are due to differences in maximum bubble radius. Maximum compressive strain exhibits a relatively weak dependence on shear modulus in low-elasticity media ($G < 100 \, \mathrm{kPa}$), and as shear modulus increases, compressive strain decreases.

Waveform peak negative pressure

Figures 14, 15 and 16 illustrate the time history of the bubble radius, maximum radial compressive/tensile stress and maximum radial compressible (Hencky) strain experienced by Lagrangian particles starting different distances away from the bubble for $p_A = 20$, 30, 40, 50 and 60, holding all other properties at their baseline values. Equivalently, this corresponds to varying the non-dimensional pressure amplitude holding all other dimensionless parameters fixed.

Increasing the peak negative pressure enhances bubble growth: the maximum radius and time at collapse (time from the beginning of growth to R_{\min}) increases linearly with pressure amplitude. Maximum compressive and tensile stresses, as well as maximum compressive (Hencky) strains, are largest at the bubble wall and monotonically decrease with increasing initial distance. Kinks in the maximum compressive stress are observed in the 20-, 30- and 40-MPa traces. This finding indicates that waveform parameters can also affect the origin (elastic vs. viscous) of stresses at different distances from the bubble wall, likely through their effects on R_{max} . When peak negative pressure is varied, the stress behavior is a consequence of the qualitatively similar bubble dynamics at each pressure. In contrast, changes in material properties can produce changes in bubble radius histories that are not simply proportional to the altered parameter.

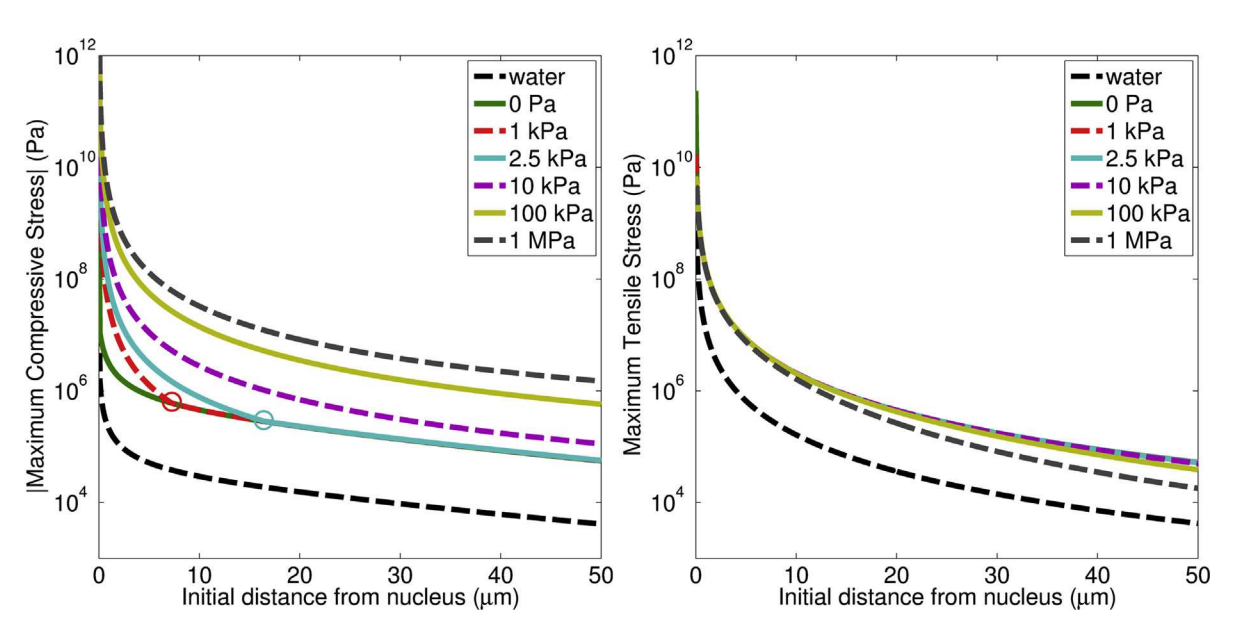


Fig. 12. Maximum compressive (left) and tensile (right) stresses as a function of initial distance from the bubble nucleus for media of different shear moduli (G = 0, 1, 2.5, 10, 100 and 1000 kPa). Elastic-to-viscous transitions are circled on compressive stress traces.

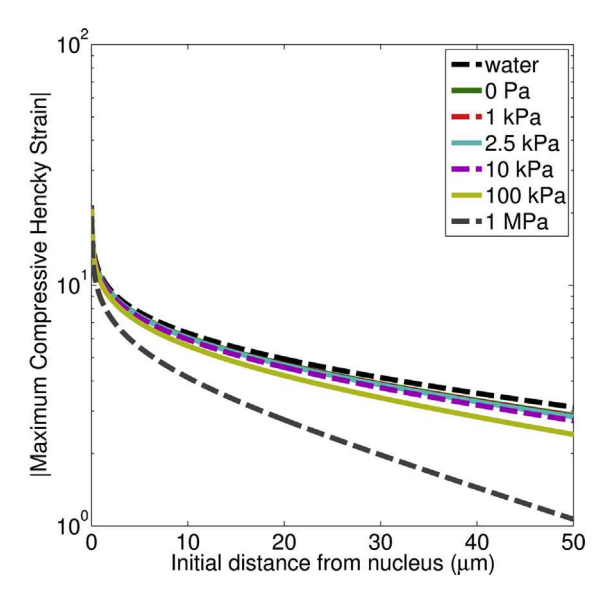


Fig. 13. Maximum compressive Hencky strain as a function of distance from the bubble nucleus in media of different shear moduli (G = 0, 1, 2.5, 10, 100 and 1000 kPa).

Waveform frequency

Figures 17, 18 and 19 illustrate the time history of the bubble radius, maximum radial compressive/tensile stress and maximum radial compressible (Hencky) strain experienced by Lagrangian particles starting different distances away from the bubble for $\omega = 0.5, 0.7, 1.0, 3.0$ and 5.0 MHz, holding all other properties constant. Equivalently, this corresponds to varying the dimensionless frequency holding all other dimensionless parameters fixed.

Decreased pulse frequency enhances bubble growth as the tension driving bubble growth acts for a longer time. As a result, larger maximum radii and collapse times (from R_{max} to R_{min}) are achieved with decreasing frequency. For the maximum tensile stress and compressive strain, these decreases are monotonic: At a given location, the stress and strain decrease with increasing frequency. As when previous parameters were varied,

"kinks" are observed in the maximum compressive stress for $\omega = 0.7, 1.0, 3.0$ and 5.0 MHz, marking the location at which the dominant stress contribution changes from elastic to viscous. Because of the smaller $R_{\rm max}$, elastic contributions decrease rapidly and are overwhelmed by viscous stresses closer to the bubble wall.

Initial nucleus size

Figures 20, 21 and 22 illustrate the time history of the bubble radius, maximum radial compressive/tensile stress and maximum radial compressible (Hencky) strain experienced by Lagrangian particles starting different distances away from the bubble, for $R_0 = 2.5, 5.0, 10, 100, 1000$ and 10,000 nm, holding other parameters at their baseline values. In terms of dimensionless parameters, varying the initial nucleus size modifies the Reynolds and Weber numbers, as well as the dimensionless frequency.

Increasing the initial nucleus size enhances bubble growth. As a result, larger maximum radii, minimum radii and collapse times (from R_{max} to R_{min}) are achieved with increasing initial bubble radius. For smaller nuclei $(R_0 < 10 \text{ nm})$, small increases in nucleus size can produce large increases in maximum bubble radius. When nucleus sizes are increased to 10- μ m initial radius, the minimum bubble radius becomes sufficient to permit additional cycles of bubble growth and collapse. A more detailed consideration of bubble behavior at and following R_{\min} is beyond the scope of the present study; however, experiments cannot rule out the possibility of additional bubble oscillations caused by limitations in temporal resolution (Vlaisavljevich et al. 2015c). Because the initial bubble radii vary, the initial distance from the radius starts from different locations on the graph. Except for the 2.5-nm case, for which values are noticeably lower, the maximum compressive/tensile stresses and the maximum compressive strain exhibit only a weak dependence on the initial radius. The stresses exhibit different behavior close to the bubble wall for micron-sized initial radii. The higher tensile stresses are explained by the finding that

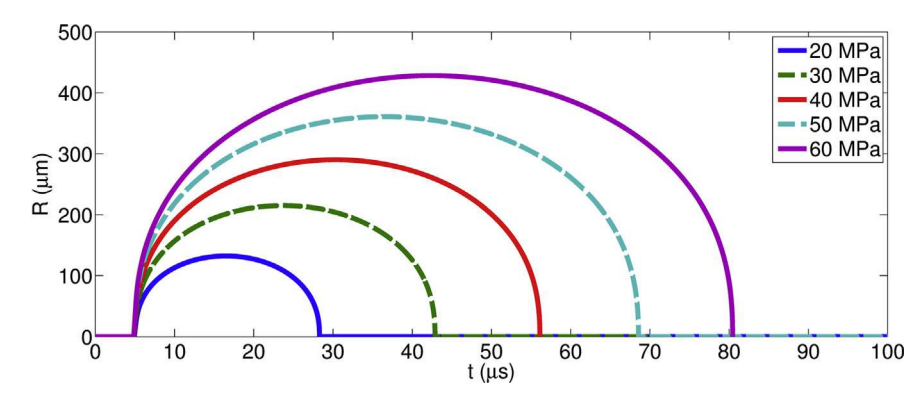


Fig. 14. Time history of the bubble radius for different peak negative pressures ($p_A = 20, 30, 40, 50$ and 60 MPa).

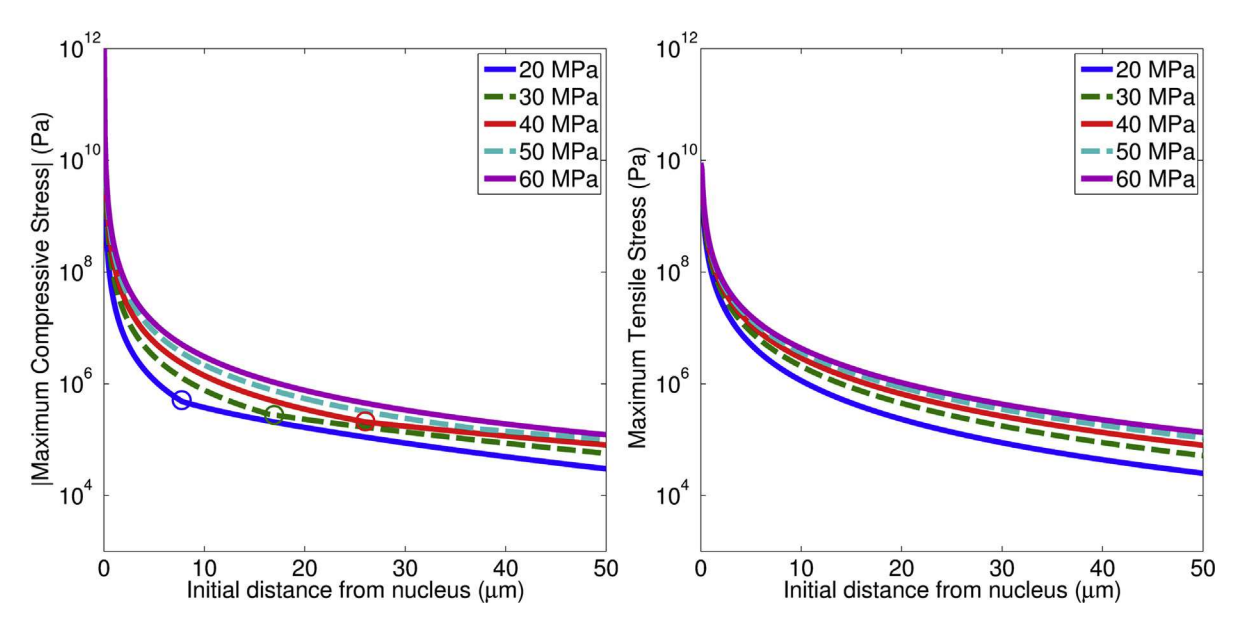


Fig. 15. Maximum compressive (left) and tensile (right) stresses as a function of initial distance from the bubble nucleus for different peak negative pressures (p_A = 20, 30, 40, 50 and 60 MPa). Elastic-to-viscous transitions are circled on compressive stress traces.

elastic stress is no longer purely compressive and contributes a significant tensile component at collapse. The appearance of elastic tensile stress at larger initial nucleus sizes occurs because larger nuclei lead to significantly smaller minimum radii. These observations can also be understood by considering the maximum values of each elastic term on the right side of eqn (3): the first term is tensile, whereas the second is compressive. Thus, for smaller initial nuclei, $R_{\rm max}/R_0 > R_0/R_{\rm min}$ and the dominant elastic contribution is compressive at maximum bub-

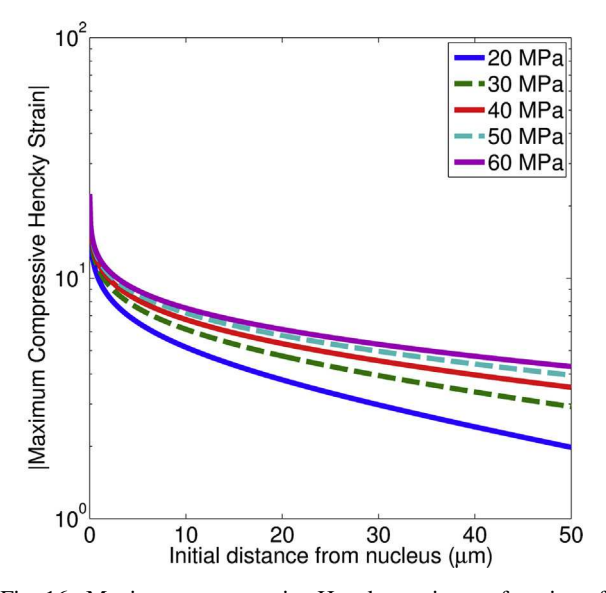


Fig. 16. Maximum compressive Hencky strain as a function of distance from the bubble nucleus for different peak negative pressures (p_A = 20, 30, 40, 50 and 60 MPa).

ble radius, whereas for larger initial radii, $R_{\rm max}/R_0 < R_0/R_{\rm min}$ and the dominant elastic contribution is tensile at collapse. Although the relative contributions of compressive stress to total stress differ significantly in small versus large nuclei, the relationships between compressive elastic and compressive viscous stresses are similar to those discussed in previous sections. Kinks indicating a transition from dominant elastic to dominant viscous compressive stress are again present in the maximum compressive stress plots and vary with maximum bubble radius; thus, the smallest growth case ($R_0 = 2.5$ nm) has a kink located significantly closer to the bubble wall.

Elastic-to-viscous stress transition

In each parameter variation study, the presence of "kinks" has been noted in certain compressive stress traces which indicate the distance of a Lagrangian particle from the bubble nucleus at which the viscous (rather than elastic) component becomes the dominant contribution to compressive stress. In other words, cells whose initial position is less than this distance experience elastic stress as an absolute maximum compressive stress, whereas cells whose initial position is greater than this distance experience viscous stress as the larger compressive stress. This elastic-toviscous transition distance location, x_{EV} , could provide a means of identifying regions dominated by elastic versus viscous effects (or strain magnitude vs. rate) in therapeutic ultrasound lesions. The dependence of x_{EV} on viscosity and shear modulus, as well as on waveform peak negative pressure and frequency, is illustrated in Figures 23 and 24, respectively, where $x_{\rm EV}$ is determined by calculating the

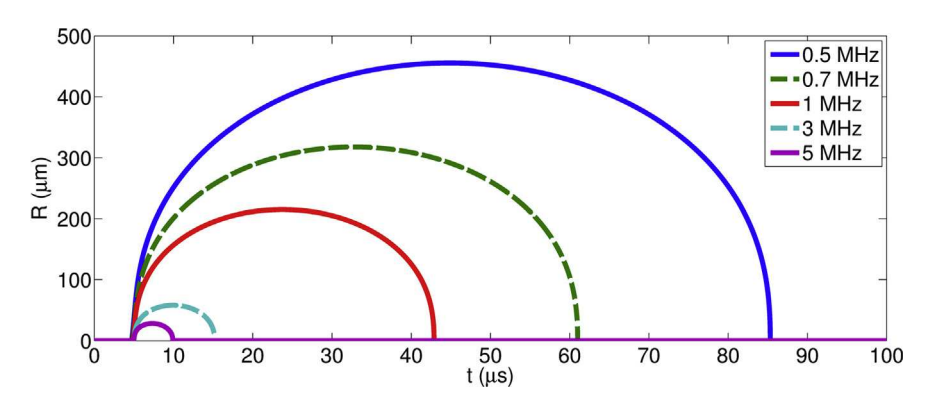


Fig. 17. Time history of the bubble radius for different frequencies ($\omega = 0.5, 0.7, 1.0, 3.0$ and 5.0 MHz).

distance at which the second spatial derivative of compressive stress becomes discontinuous. All parameters are varied about the baseline. The elastic-to-viscous transition distance strongly depends on μ and G, as it decreases with increasing viscosity, but increases with increasing shear modulus; $x_{\rm EV}$ decreases with increasing frequency, but increases (linearly) with increasing amplitude as expected based on the dependence of $R_{\rm max}$ on those properties.

DISCUSSION

Experimental studies suggest that tissue properties play a key role in determining tissue susceptibility to cavitation generation and histotripsy-induced tissue damage (Vlaisavljevich et al. 2013). Our results highlight the importance of elasticity, viscosity, peak negative pressure and waveform frequency to hypothesized mechanical tissue damage mechanisms. An improved understanding of

cavitation damage mechanisms will help predict damage susceptibility of different tissues, as well as differential damage responses within a focal region under different acoustic parameters. This knowledge can ultimately be used to guide safety considerations and enable treatment planning.

Figure 25 and Table 2 illustrate the relationships between the maxima in total stress, strain and strain rate by highlighting three key points during a single cycle of bubble growth and collapse that correspond to relative or absolute maxima in these field quantities. First, a tensile histotripsy pulse drives the onset of explosive bubble growth when $R = R_0$. At this time, viscous effects predominate and both the strain rate and compressive stress achieve relative maxima. At distances greater than $x_{\rm EV}$ (the elastic-to-viscous transition point), this maximum in compressive viscous stress at the onset of bubble growth will also contribute the absolute maximum total

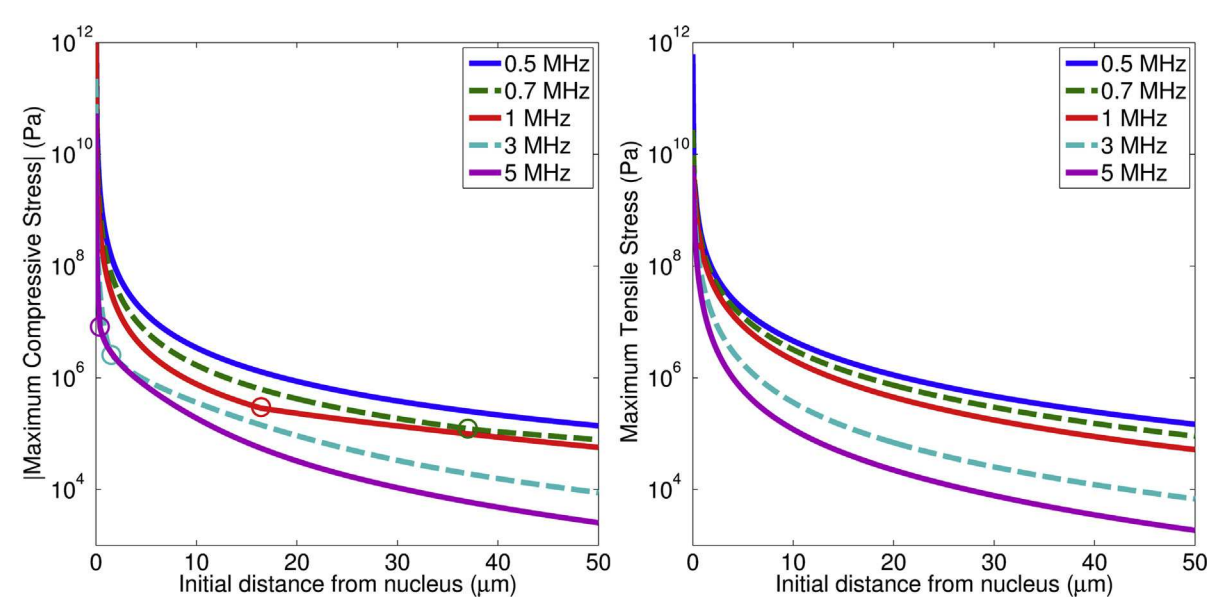


Fig. 18. Maximum compressive (left) and tensile (right) stresses as a function of distance from the bubble nucleus for different frequencies (ω = 0.5, 0.7, 1.0, 3.0 and 5.0 MHz). Elastic-to-viscous transitions are circled on compressive stress traces.

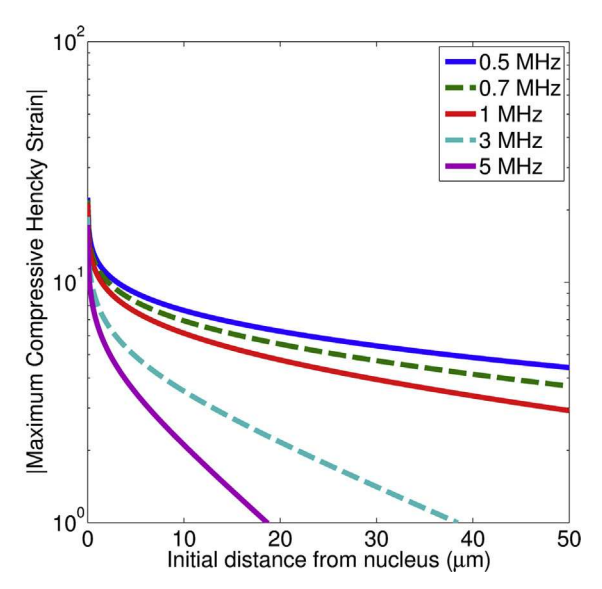


Fig. 19. Maximum compressive Hencky strain as a function of distance from the bubble nucleus for different frequencies ($\omega = 0.5, 0.7, 1.0, 3.0$ and 5.0 MHz).

compressive stress during the life span of the bubble. Next, bubble growth proceeds rapidly until viscous resistance and tissue stiffness limit growth to a maximum radius, $R = R_{\text{max}}$. Here, tissue elasticity has the dominant influence on bubble dynamics. Both the compressive stress and compressive strain are maximized, whereas the strain rate and viscous stress are negligible. At distances less than x_{EV} , this maximum in compressive elastic stress contributes the absolute maximum total compressive stress over the life span of the bubble. Finally, the bubble undergoes a violent collapse to a minimum radius $R_{\min} < R_0$. At minimum radius, viscous effects again dominate, and tensile stress, tensile strain, and strain rate are all maximized. Tensile stress is purely viscous in origin and contributes the absolute maximum total stress when viscosity is sufficiently large.

These maxima in field quantities are also affected by waveform parameters that change the underlying bubble

dynamics. Specifically, any change in waveform frequency or pressure amplitude that changes R_0 , R_{max} or $R_{\rm min}$ can also change the stresses and strains. First, increases in pressure amplitude permit greater bubble growth, increasing R_{max} . This will produce proportional increases in maximum compressive stress and strain, as well as relatively smaller increases in tensile stress. In contrast, increases in frequency limit bubble growth and, thus, decrease the maximum compressive stress and strain. Waveform parameters can also affect x_{EV} . Increases in pressure amplitude and decreases in frequency result in smaller $x_{\rm EV}$ values, indicating that the elastic compressive stress at R_{max} is exceeded by viscous compressive stress at the onset of bubble growth closer to the bubble wall in these reduced growth cases. Additionally, tensile strains at bubble collapse far exceeded the ultimate fractional strains measured for soft tissue, but were nearly instantaneous and more localized to the bubble wall than compressive strains. Further study is needed to clarify their relevance to strain-related tissue damage. More readily understood is the observation that maximum compressive strain occurs at maximum radius when the tissue is under greatest deformation and coincides with a maximum in compressive (purely elastic) stress, thus supporting the hypothesis that maximum radius is a relevant parameter for mechanical tissue damage.

Predicting the elastic-to-viscous transition

Stress is hypothesized to play an important role in tissue damage produced by high-amplitude ultrasound therapies. In a study of tissue mechanical properties and susceptibility to perforation, undamaged tissues were observed to have higher ultimate tensile strength, thus suggesting that higher ultimate tensile stress was more predictive of tissue resistance to damage than high ultimate strain (Vlaisavljevich et al. 2013). These observations motivate further study of the relationship between stress and tissue damage; however, stress fields are difficult to measure under highly transient loading. A means

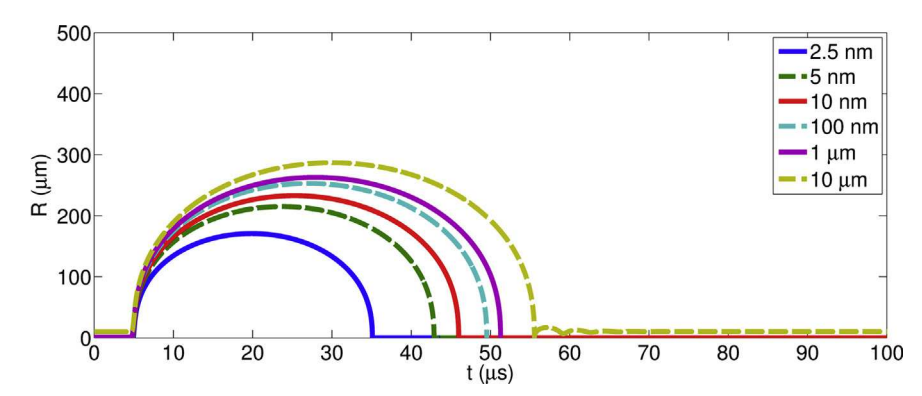


Fig. 20. Time history of the bubble radius for different initial bubble radii ($R_0 = 2.5, 5.0, 10, 100, 1000 \text{ and } 10,000 \text{ nm}$).

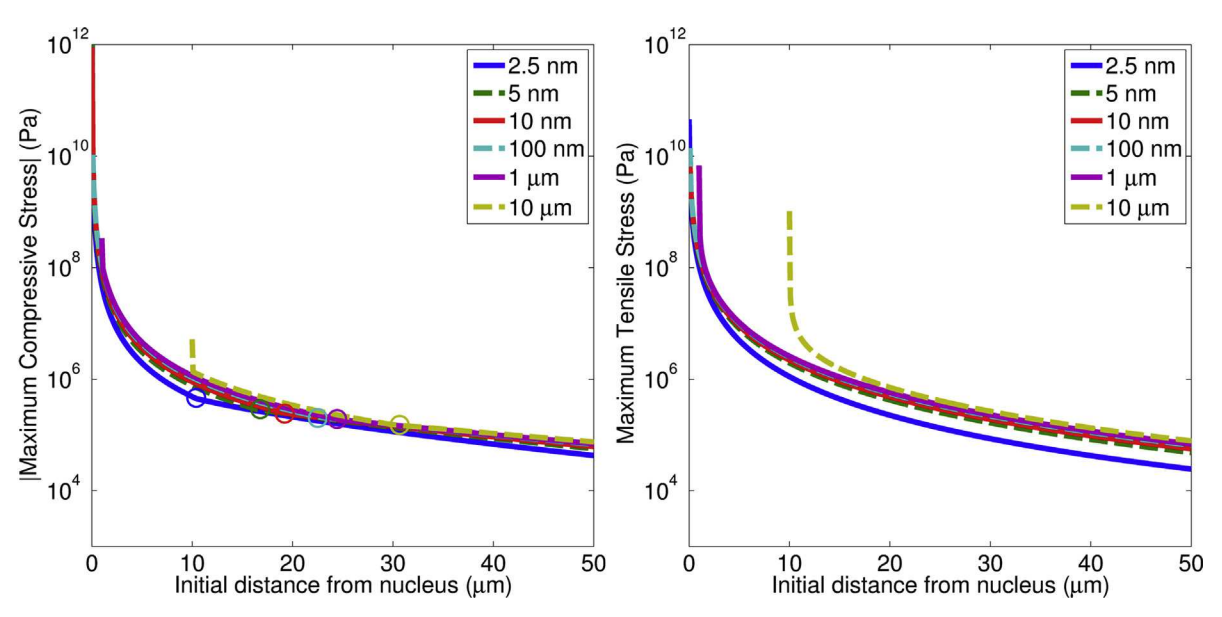


Fig. 21. Maximum compressive (left) and tensile (right) stresses as a function of initial distance from the bubble nucleus for different initial bubble radii ($R_0 = 2.5, 5.0, 10, 100, 1000 \text{ and } 10,000 \text{ nm}$). Elastic-to-viscous transitions are circled on compressive stress traces.

of relating salient features of the stress field to more measurable parameters could improve understanding of stress-related damage mechanisms.

One potential means of characterizing stress fields is by the predominance of viscous versus elastic stress characteristics. Fundamentally, elastic stress depends on the tissue deformation (strain), and viscous stress is directly proportional to strain rate. Thus, the elastic-to-viscous

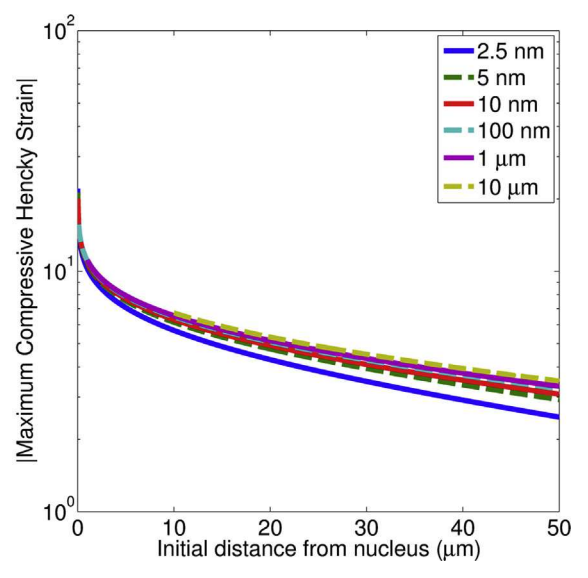


Fig. 22. Maximum compressive Hencky strain as a function of distance from the bubble nucleus for different initial bubble radii ($R_0 = 2.5, 5.0, 10, 100, 1000 \text{ and } 10,000 \text{ nm}$).

stress transition distance, x_{EV} , introduces a spatial dependence on the relevance of strain versus strain rate in observed tissue damage. Recent experimental studies suggest that strain and strain rate have different effects on cell injury (Bar-Kochba et al. 2016): Strain rate was found to affect injury morphology and the extent of cell death across a population, whereas compressive strain determined the time to cell death. It is thus reasonable to expect that tissue regions dominated by either strain or strain rate effects will give rise to distinct patterns of injury. Prediction of x_{EV} could thus be used to predict the spatial extent of these distinct histopathologies, as long as the material models are sufficiently accurate. The monotonic results in Figures 23 and 24 suggest that an analytical expression for $x_{\rm EV}$ may be achievable. One might expect that x_{EV} , properly scaled, should depend on the relative magnitude of elastic forces ($\sim G\delta^2$) to viscous forces $(\sim \mu \nu \delta)$, where δ and ν are characteristic lengths and velocities corresponding to the deformation magnitude and rate. The relevant length describing deformations is $R_{\rm max}$, the point at which the tissue is under maximum deformation. The relevant velocity characterizing the growth is expected to depend on the pressure amplitude, for example, $\sqrt{p_{\rm A}/\rho_{\infty}}$. Thus, defining the dimensionless elastic-to-viscous forces ratio

$$\xi = \frac{GR_{\text{max}}}{\mu \sqrt{\rho_{\text{A}}/\rho_{\infty}}} \tag{10}$$

it is expected that the properly scaled transition location obeys the relation

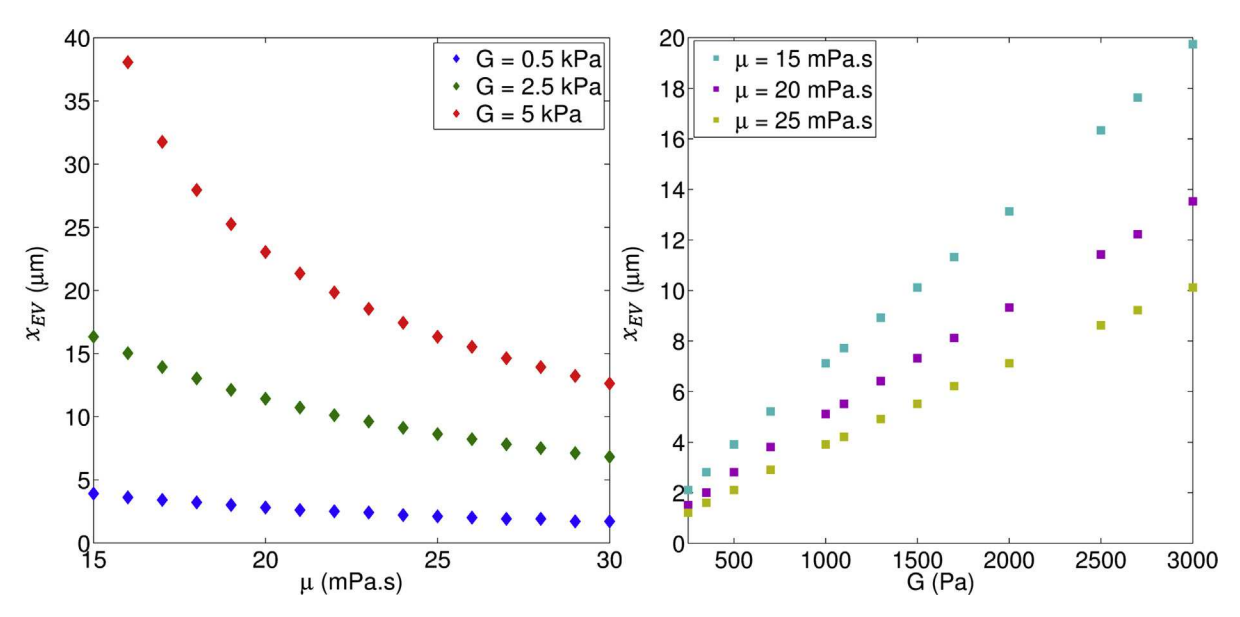


Fig. 23. Elastic-to-viscous compressive stress transition distance x_{EV} as a function of viscosity for G = 0.5, 2.5 and 5 kPa (left) and of shear modulus for $\mu = 15, 20$ and 25 mPa·s (right).

$$\frac{x_{\rm EV}}{R_{\rm max}} = f(\xi) \tag{12}$$

where f is some function of ξ . To investigate this scaling, $x_{\rm EV}/R_{\rm max}$ is plotted versus ξ in Figure 26 by including all of the data from Figures 23 and 24.

The results are unambiguous: For the parameter range under consideration, all of the data collapse onto a single curve, thus verifying the validity of the scaling of eqn (10). Moreover, for $\xi \in [0,0.27]$, the relationship is linear, such that

where $c \approx 0.4$ by data fit. Because ξ represents the ratio of elastic to viscous forces, the increase in $x_{\rm EV}/R_{\rm max}$ with ξ is understandable: As the relative importance of elastic stresses increases compared with the viscous contribution (increasing ξ), for example, because of increased shear modulus relative to viscosity, the region in which elastic effects dominate extends farther from the bubble wall. The linear dependence on ξ , and thus on $R_{\rm max}$, in

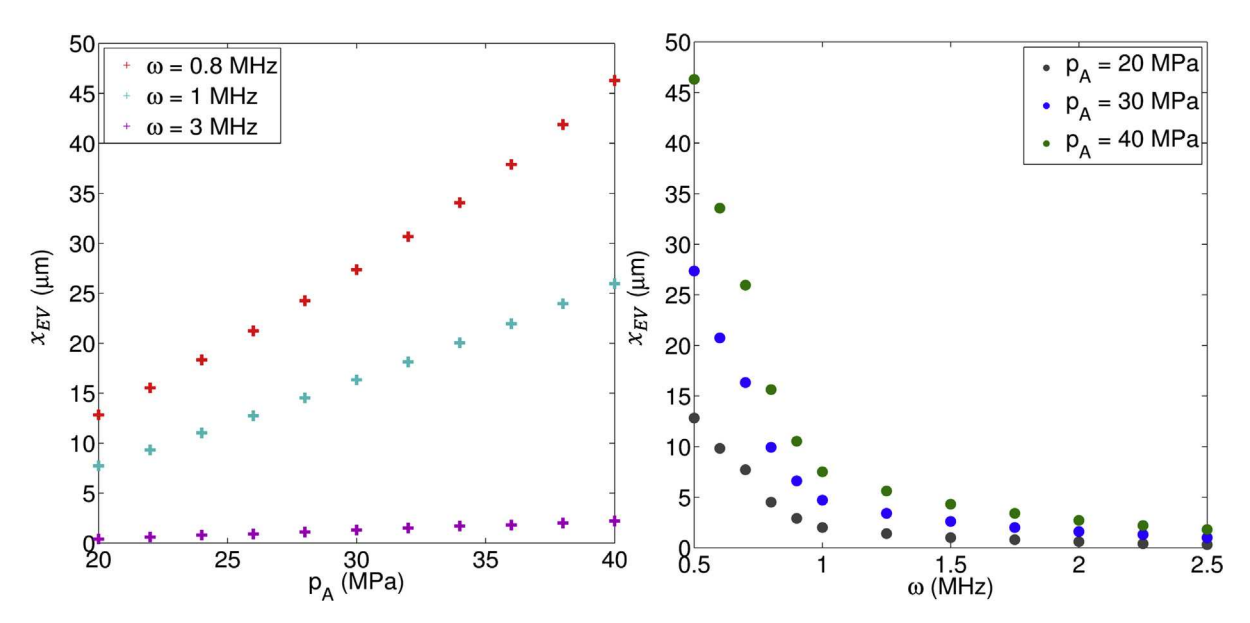


Fig. 24. Elastic-to-viscous compressive stress transition distance $x_{\rm EV}$ as a function of peak negative pressure for $\omega = 0.8$, 1.0, and 3.0 MHz (left) and of waveform frequency for $p_{\rm A} = 20$, 30 and 40 MPa (right).

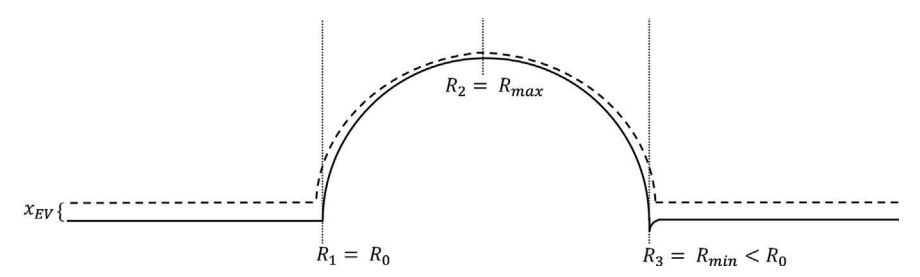


Fig. 25. Schematic illustrating three likely time points for mechanical tissue damage during a single cycle of bubble growth and collapse. The dominant mechanisms acting at points R_1 , R_2 and R_3 are given in Table 2.

[0,0.27] indicates that the size of the region dominated by elastic stresses increases in a geometrically similar fashion.

For the larger shear modulus cases with low viscosity (G = 5 kPa and $\mu < 20$ mPa·s, red diamond in Fig. 26), as well as the lowest frequency ($\omega = 0.8$ MHz), the scaled transition location increases more rapidly with increasing ξ , such that $x_{\rm EV}/R_{\rm max}$ no longer obeys a linear relationship; the data collapse is not as clear. These deviations reflect the predominance of elastic over viscous effects. For low frequency with equivalent viscoelastic parameters, the dominance of elasticity on overall dynamics occurs because bubble growth in these large deformation cases is limited more by tissue resistance to further deformation than by viscous dissipation. The authors recognize that for the scaling in eqn (10) to be practically relevant, a corresponding scaling for R_{max} or perhaps R_{max}/R_0 is necessary, though it lies beyond the scope of the present study and has been investigated by others (Bader and Holland 2016).

CONCLUSIONS

We studied the effects of tissue properties (viscosity, shear modulus, nucleus size) and waveform parameters (peak negative pressure, frequency) on the bubble dynamics of a 5-nm nucleus subjected to a single negative histotripsy-relevant cycle. The resulting stress and strain fields in the surrounding medium, modeled via a Kelvin–Voigt viscoelastic constitutive relation with non-linear elasticity, were examined in the light of potential tissue injury. Overall, the largest radial stresses were experienced at the bubble wall and are due to different mechanisms: while the largest tensile stress

was of viscous origin and occurred at collapse, two peaks in compressive stress occurred at initial growth (viscous) and maximum radius (elastic). The maximum stresses/strains depended on the tissue and waveform properties: In addition to affecting the stresses/strains via the bubble dynamics (as do the waveform properties and nucleus size), the viscosity and shear modulus also dictated the dependence on strain magnitude and rate. The stresses and strains decreased with depth into the tissue, though the viscous and elastic contributions decreased at different rates. Elastic stresses produced maximum compressive stress for cells initially near the bubble and viscous stresses dominated farther away. There was thus a critical initial distance from the nucleus beyond which the maximum compressive stress experienced by those cells is of viscous origin. Scaling analysis was used to illustrate that a fundamental relationship exists between the scaled transition location and the dimensionless elastic-to-viscous forces ratio, which was linear for most of the parameter range. This result further indicated that the size of the region dominated by elastic stresses increases in a geometrically similar fashion. Thus, assuming that stresses/strains are the dominant mechanisms of cavitation-induced tissue damage, our results support the potential value of using maximum bubble radius as a metric for tissue damage, especially if this metric includes dependence on tissue viscosity, elasticity and waveform parameters.

Given the fundamental nature of the present problem, our results can be generalized. However, they are limited to the material model under consideration. The chosen model accounts for important features of soft tissue mechanics (finite deformation, viscoelasticity), but

Table 2. Mechanical damage mechanisms during a single cycle of bubble growth and collapse for nucleus sizes <10 nm

$R_1 = R_0$	$R_2 = R_{\text{max}}$	$R_3 = R_{\min} < R_0$
Viscous effects dominate	Elastic effects dominate	Viscous effects dominate
Maximum compressive stress	Maximum compressive stress	Maximum tensile stress
(absolute maximum for $x > x_{EV}$)	(absolute maximum for $x < x_{EV}$)	Maximum tensile strain
Maximum strain rate	Maximum compressive strain (absolute)	Maximum strain rate

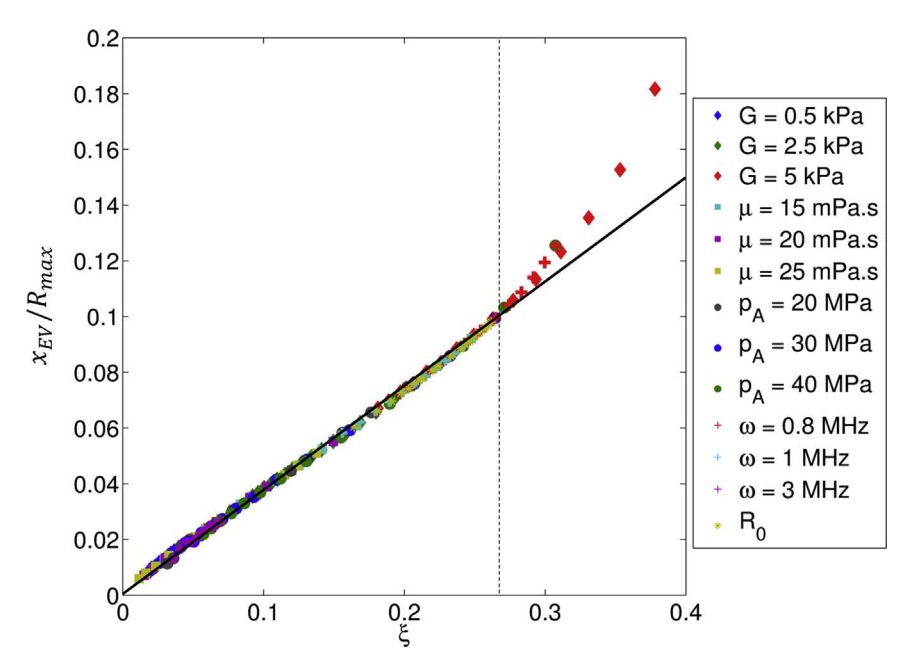


Fig. 26. Scaled elastic-to-viscous compressive stress transition distance as a function of the dimensionless elastic-to-viscous forces ratio, ξ .

the complex microstructure may require more sophisticated constitutive relations for accurate, quantitative stress predictions. Bubble–bubble interactions could also influence the damage mechanisms postulated in this study. Thermodynamics and transport phenomena in soft tissue are not well understood; mass transport inside (Barajas and Johnsen 2017) and outside the bubble may affect bubble growth. Strategies to improve the fidelity of the models are underway and require experimental characterization of soft tissue.

Acknowledgements—This work was supported by grants from the National Science Foundation (CBET 1253157); National Institute of Biomedical Imaging and Bioengineering (NIBIB), National Institutes of Health, under Award R01EB008998; National Institute of Neurological Disorders and Stroke (NINDS), National Institutes of Health, under Award R21NS093121; a Research Scholar Grant from the American Cancer Society (RSG-13-101-01-CCE); and The Hartwell Foundation.

REFERENCES

Allen JS, Roy RA. Dynamics of gas bubbles in viscoelastic fluids: I. Linear viscoelasticity. J Acoust Soc Am 2000a;107:3167–3178.

Allen JS, Roy RA. Dynamics of gas bubbles in viscoelastic fluids: II. Nonlinear viscoelasticity. J Acoust Soc Am 2000b;108:1640–1650. Bader KB, Holland CK. Predicting the growth of nanoscale nuclei by histotripsy pulses. Phys Med Biol 2016;61:2947.

Bailey M, Cleveland R, Colonius T, Crum L, Evan A, Lingeman J, McAteer JA, Sapozhnikov O, Williams JC. Cavitation in shock wave lithotripsy: the critical role of bubble activity in stone breakage and kidney trauma. Proc IEEE Int Symp Ultrason 2003;1:724–727.

Bar-Kochba É, Scimone MT, Estrada JB, Franck C. Strain and rate-dependent neuronal injury in a 3D in vitro compression model of traumatic brain injury. Sci Rep 2016;6:30550.

Barajas C, Johnsen E. The effects of heat and mass transfer on freely oscillating bubbles in a viscoelastic, tissue-like medium. J Acoust Soc Am 2017;141:908.

Brujan E. Cavitation in non-Newtonian Fluids: With biomedical and bioengineering applications. Berlin/Heidelberg: Springer Science & Business Media; 2010.

Church CC, Yang X. A theoretical study of gas bubble dynamics in tissue. In: Innovations in nonlinear acoustics: ISNA17—17th international symposium on nonlinear acoustics including the International Sonic Boom Forum, Vol. 838. College Park, MD: American Institute of Physics; 2006. p. 217–224.

De S, Rosen J, Dagan A, Hannaford B, Swanson P, Sinanan M. Assessment of tissue damage due to mechanical stresses. Int J Robot Res 2007;26:1159–1171.

Diamond SL. Engineering design of optimal strategies for blood clot dissolution. Annu Rev Biomed Eng 1999;1:427–461.

Duck FA. Physical properties of tissues: A comprehensive reference book. London: Academic Press; 2013.

Duryea AP, Cain CA, Roberts WW, Hall TL. Removal of residual cavitation nuclei to enhance histotripsy fractionation of soft tissue. IEEE Trans Ultrason Ferroelectr Freq Control 2015;62:2068–2078.

Gaudron R, Warnez M, Johnsen E. Bubble dynamics in a viscoelastic medium with nonlinear elasticity. J Fluid Mech 2015;766:54–75.

Harvey EN, Barnes D, McElroy WD, Whiteley A, Pease D, Cooper K. Bubble formation in animals: I. Physical factors. J Cell Comp Physiol 1944;24:1–22.

Hua C, Johnsen E. Nonlinear oscillations following the Rayleigh collapse of a gas bubble in a linear viscoelastic (tissue-like) medium. Phys Fluids 2013;25:083101.

Keller JB, Miksis M. Bubble oscillations of large amplitude. J Acoust Soc Am 1980;68:628–633.

Khanafer K, Schlicht M, Berguer R. How should we measure and report elasticity in aortic tissue? Eur J Vasc Endovasc Surg 2013;45: 332–339.

Maxwell AD, Cain CA, Hall TL, Fowlkes JB, Xu Z. Probability of cavitation for single ultrasound pulses applied to tissues and tissue-mimicking materials. Ultrasound Med Biol 2013;39: 449–465.

Miller DL, Smith NB, Bailey MR, Czarnota GJ, Hynynen K, Makin IRS. American Institute of Ultrasound in Medicine Bioeffects Committee. Overview of therapeutic ultrasound applications and safety considerations. J Ultrasound Med 2012;31:623–634.

Noltingk BE, Neppiras EA. Cavitation produced by ultrasonics. Proc Phys Soc B 1950;63:674.

- Nyborg W, Carson P, Carstensen E, Dunn F, Miller D, Miller M, Thompson H, Ziskin M. Exposure criteria for medical diagnostic ultrasound: II. Criteria based on all known mechanisms. Bethesda, MD: National Council on Radiation Protection and Measurements; 2002
- Parsons JE, Cain CA, Abrams GD, Fowlkes JB. Pulsed cavitational ultrasound therapy for controlled tissue homogenization. Ultrasound Med Biol 2006;32:115–129.
- Plesset M. The dynamics of cavitation bubbles. J Appl Mech 1949;16: 277–282.
- Roberts WW, Hall TL, Ives K, Wolf JS, Fowlkes JB, Cain CA. Pulsed cavitational ultrasound: A noninvasive technology for controlled tissue ablation (histotripsy) in the rabbit kidney. J Urol 2006;175:734–738.
- Shampine LF, Reichelt MW. The MATLAB ode suite. SIAM J Sci Comput 1997;18:1–22.
- Shima A, Tsujino T. On the dynamics of bubbles in polymer aqueous solutions. Appl Sci Res 1982;38:255–263.
- Vlaisavljevich E, Kim Y, Owens G, Roberts W, Cain C, Xu Z. Effects of tissue mechanical properties on susceptibility to histotripsy-induced tissue damage. Phys Med Biol 2013;59:253.
- Vlaisavljevich E, Maxwell A, Warnez M, Johnsen E, Cain C, Xu Z. Histotripsy-induced cavitation cloud initiation thresholds in tissues of different mechanical properties. IEEE Trans Ultrason Ferroelectr Freq Control 2014;61:341–352.
- Vlaisavljevich E, Aydin O, Lin KW, Durmaz YY, Fowlkes B, ElSayed M, Xu Z. The role of positive and negative pressure on cavitation nucleation in nanodroplet-mediated histotripsy. Phys Med Biol 2015a;61:663.
- Vlaisavljevich E, Lin KW, Maxwell A, Warnez MT, Mancia L, Singh R, Putnam AJ, Fowlkes B, Johnsen E, Cain C, Xu Z. Effects of ultra-

- sound frequency and tissue stiffness on the histotripsy intrinsic threshold for cavitation. Ultrasound Med Biol 2015b;41:1651–1667.
- Vlaisavljevich E, Lin KW, Warnez MT, Singh R, Mancia L, Putnam AJ, Johnsen E, Cain C, Xu Z. Effects of tissue stiffness, ultrasound frequency, and pressure on histotripsy-induced cavitation bubble behavior. Phys Med Biol 2015c;60:2271.
- Vlaisavljevich E, Maxwell A, Mancia L, Johnsen E, Cain C, Xu Z. Visualizing the histotripsy process: Bubble cloud–cancer cell interactions in a tissue-mimicking environment. Ultrasound Med Biol 2016a;42:2466–2477.
- Vlaisavljevich E, Xu Z, Maxwell AD, Mancia L, Zhang X, Lin KW, Duryea AP, Sukovich JR, Hall TL, Johnsen E, Cain CA. Effects of temperature on the histotripsy intrinsic threshold for cavitation. IEEE Trans Ultrason Ferroelectr Freq Control 2016b;63: 1064–1077
- Warnez M, Johnsen E. Numerical modeling of bubble dynamics in viscoelastic media with relaxation. Phys Fluids 2015;27: 063103.
- Wells RE Jr, Merrill EW. Influence of flow properties of blood upon viscosity–hematocrit relationships. J Clin Invest 1962;41:1591.
- Xiao H. Hencky strain and Hencky model: Extending history and ongoing tradition. Multidiscipline Model Mater Struct 2005;1:1–52.
- Xu Z, Fowlkes JB, Rothman ED, Levin AM, Cain CA. Controlled ultrasound tissue erosion: The role of dynamic interaction between insonation and microbubble activity. J Acoust Soc Am 2005;117: 424–435.
- Yang X, Church CC. A model for the dynamics of gas bubbles in soft tissue. J Acoust Soc Am 2005;118:3595–3606.
- Zimberlin JA, Sanabria-DeLong N, Tew GN, Crosby AJ. Cavitation rheology for soft materials. Soft Matter 2007;3:763–767.